Tools for creating wide-field views of the human retina using Optical Coherence Tomography

Ashavini M. Pavaskar
Marquette University

TOOLS FOR CREATING WIDE-FIELD VIEWS OF THE HUMAN RETINA USING OPTICAL COHERENCE TOMOGRAPHY

by

Ashavini Pavaskar, B.E

A Thesis submitted to the Faculty of the Graduate School,
Marquette University,
in Partial Fulfillment of the Requirements for
the Degree of Master of Science

Milwaukee, Wisconsin

August 2011

ABSTRACT

TOOLS FOR CREATING WIDE-FIELD VIEWS OF THE HUMAN RETINA USING OPTICAL COHERENCE TOMOGRAPHY

Ashavini M. Pavaskar, B.E.

Marquette University, 2011

Optical Coherence Tomography (OCT) has allowed in-vivo viewing of details of retinal layers like never before. With the development of spectral domain OCT (SD-OCT) details of nearly 2µm axial resolution and higher imaging speed have been reported. Nevertheless, a single volume scan of the retina is typically restricted to 6mm x 6mm in size. Having a larger field of view of the retina will definitely enhance the clinical utility of the OCT.

A tool was developed for creating wide-field thickness maps of the retina by combining the use of already available tools like i2k Retina™ (DualAlign, LLC, Clifton Park, NY) and the thickness maps from Cirrus HD-OCT research browser (Carl Zeiss Meditec, Dublin, California, USA). Normal subjects (n=20) were imaged on Zeiss Cirrus HD-OCT using 512x128 Macular Cube scanning protocol. Sixteen overlapping volumetric images were obtained by moving the internal fixation target around such that the final stitched maps were 12mm x 14mm in size. The thickness maps were corrected for inter-individual differences in axial lengths measured using Zeiss IOL Master and averaged to obtain a normative map.

An algorithm was also developed for montaging 3-D volume scans. Using this algorithm two OCT volume scans can be registered and stitched together to obtain a larger volume scan. The algorithm can be described as a two step process involving 3-D phase-correlation and 2-D Pseudo-polar Fourier transform (PPFT). In the first step, 3-D phase-correlation provides translation values in the x, y and z axis. The second step involves applying PPFT on each overlapping pair of B-scans to find rotation in the x-y plane. Subsequent volumes can be stitched to obtain a large field of view.

We developed a simple and robust method for creating wide-field views of the retina using existing SD-OCT hardware. As segmentation algorithms improve, this method could be expanded to produce wide-field maps of retinal sub-layers, such as the outer nuclear layer or retinal nerve fiber layer. These wide-field views of the retina may prove useful in evaluating retinal diseases involving the peripheral retina (*e.g.*, retinitis pigmentosa and glaucoma).

ACKNOWLEDGEMENTS

I would like to express my gratitude to my thesis advisor Dr. Joseph Carroll for his invaluable guidance throughout my thesis. His insight, encouragement and immense knowledge in the field have helped me in my research as well as in being a more motivated individual.

I would like to thank Dr. Taly Gilat-Schmidt and Dr. Kristina Ropella for serving as members of my thesis committee and providing valuable feedback. I would like to acknowledge my funding sources, NIH, The Gene and Ruth Posner foundation and Research to Prevent Blindness. Special thanks to Dr. Gehua Yang of DualAlign LLC for his help in answering my questions about i2kalign software. Special acknowledgement to all the members of the Carroll Lab including Adam Dubis, Jungtae Rha, Phyl Summerfelt, Brett Schroeder, Rob Cooper and Pooja Godara for their help and for making the lab a fun place to work in.

Finally I would like to thank my family and friends for their unending support.

TABLE OF CONTENTS

LIST OF FIGURES

ABBREVIATIONS

AMD	Age-related macular degeneration
CT	Computed tomography
DME	Diabetic macular edema
FA	Fluorescein angiography
FFT	Fast Fourier transforms
FRFT	Fractional Fourier transform
GCL	Ganglion cell layer
HWR	Homography with Radial
ICG	Indocyanine green
ICP	Iterative Closest Point
IFFT	Inverse Fourier Transform
INL	Inner Nuclear Layer
IPL	Inner plexiform layer
IS	Inner segment
LSO	Line scanning ophthalmoscope
MRI	Magnetic resonance imaging
NFL	Nerve fiber layer
OCT	Optical coherence tomography
ONH	Optic nerve head
ONL	Outer nuclear layer
OPL	Outer plexiform layer
OS	Outer segment

PET	Positron emission tomography
PPFT	Pseudo-polar Fourier transform
ROI	Region of interest
RPE	Retinal pigment epithelium
RTA	Retinal thickness analyzer
SAD	Sum of absolute differences
SD-OCT	Spectral-domain OCT
SSD	Sum of squared intensity differences
SVP	Summed volume projection
TD-OCT	Time-domain OCT
WHO	World Health Organization

1. INTRODUCTION AND SPECIFIC AIMS

Optical Coherence Tomography (OCT) is a noninvasive imaging technique that enables in-vivo cross-sectional visualization of biological tissue at micrometer resolution (Swanson, Izatt et al. 1993). Since the first demonstration of its use in imaging the retina with an axial resolution of 15µm, OCT technology has improved to a large extent, currently enabling imaging with axial resolution of up to 2µm. Standard time domain Optical Coherence Tomography (TD-OCT) has limited acquisition speed and resolution. Since longer acquisition speeds can cause image artifacts due to eye motion, 3D imaging of the retina was previously difficult. With the advancement of spectral domain OCT (SD-OCT), it is now possible to obtain three-dimensional volume scans of the retina with reasonably short acquisition times allowing us to generate two-dimensional thickness maps (Drexler 2004). Such developments have made OCT one of the fastest adopted technologies in ophthalmology for diagnosis and study of retinal pathologies.

In ophthalmology, precise visualization of pathology is especially critical for diagnosis and staging of ocular diseases (Drexler, Morgner et al. 2001). OCT on its own provides only qualitative visualization of the retina. In combination with image processing and segmentation techniques, OCT permits quantitative measurement of internal retinal architecture and morphology, providing a clinical diagnostic tool for diseases such as glaucoma, diabetic retinopathy, and macular degeneration – the three leading causes of blindness (Drexler, Morgner et al. 2001). Retinal thickness analysis is an important way to quantify pathological changes (Polaczek-Krupa and Grabska-Liberek 2006). In a clinical setting, OCT imaging typically involves taking 6mm x 6mm scans of the macula and the optic nerve head (ONH) and a number of studies have

established normative databases for the macular (Chan, Duker et al. 2006; Grover, Murthy et al. 2009) and ONH regions (Mwanza, Oakley et al. 2011). However many retinal diseases, including retinitis pigmentosa (Berson 1993) and glaucoma (Johnson 1995; Quigley 2005) affect the peripheral retina. There is a lack of normal data covering regions outside the fovea and ONH. Considering there is a trade-off between imaging area, sampling density and the acquisition time, one approach is to combine smaller high density scans to generate wide-field thickness maps and volumes. In a previous study Jacobson, Aleman et al. (2005) created wide-field retinal thickness maps for identifying intact photoreceptors in RPE65 mutations by manually combining overlapping scans. An automated technique to create such wide-field thickness maps will enhance the utility of OCT thickness maps.

Cross-sectional visualization is extremely important for diagnosis of retinal diseases like diabetic macular edema (DME) and glaucoma (Hee, Puliafito et al. 1995; Schuman, Hee et al. 1995; Hee, Baumal et al. 1996). The size of the volume that can be imaged at one time is limited by artifacts caused by motion of the subject's eye. Larger volume views need to be generated by stitching several smaller high density volume scans. In this study, using image processing techniques, tools have been developed for 2-D and 3-D wide-field viewing of retinal morphology. Accordingly, the specific aims of this project were to:

i. Develop a tool to create wide-field thickness maps of the retina and begin establishing a normative database.
ii. Develop an algorithm to stitch three-dimensional retinal volume scans for wide-field cross-sectional visualization.

2. BACKGROUND

2.1 Basics of Vision

Light enters the eye through the pupil and forms an inverted image on the retina. Fig 2.1 shows a schematic of the eye. The eye consists of three layers of tissue. The external layer is a tough white fibrous tissue called the sclera. The sclera forms a transparent tissue called cornea in front of the eye. The middle layer is comprised of the iris, the ciliary body and the choroid. The iris is a pigmented ring of tissue that regulates the amount of light entering the eye by adjusting the size of the pupil. The ciliary body supports the lens on either side and helps in altering the shape of the lens to enable focusing. The choroid is a source of blood supply to the retina composed of a mesh of capillary bed. The space between the cornea and the lens is called the anterior chamber. It is filled with a fluid called the aqueous humor which is responsible for supplying nutrients to these structures. The vitreous humor is a clear jelly like liquid that fills the large cavity between the lens and the back surface of the eye. The innermost layer of tissue is the retina. The cornea and the lens focus the incident light onto the retina, the tissue where light energy is converted to a neural signal.

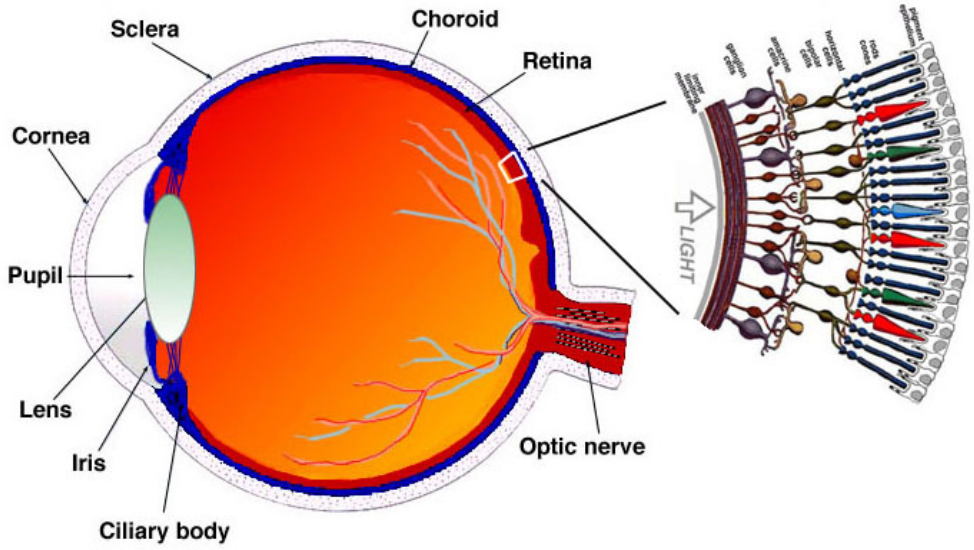

Figure 2.1: A schematic of the human eye with enlarged schematic of the retina (Image from http://webvision.med.utah.edu/)

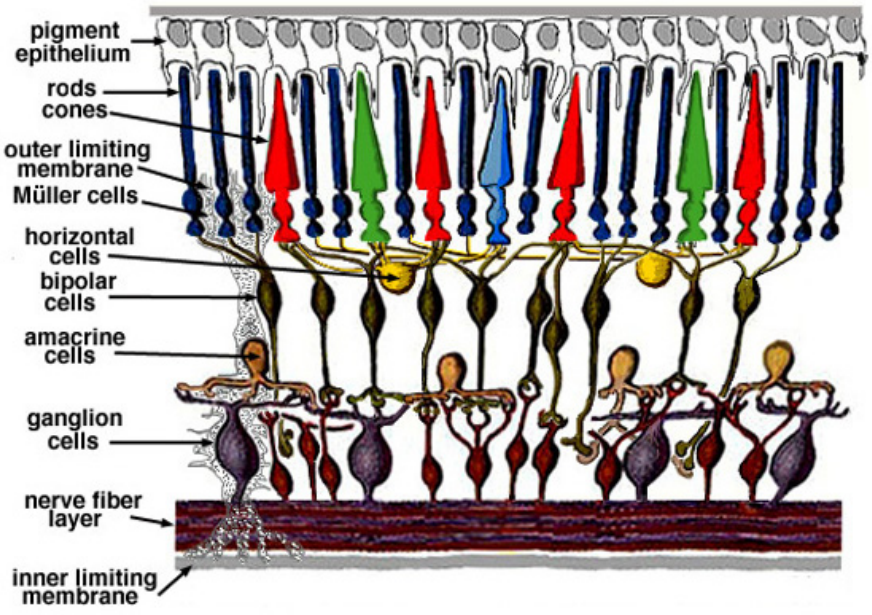

Figure 2.2: Schematic showing different layers of the retina (Image from http://webvision.med.utah.edu/)

The retina is a highly layered structure approximately 0.3mm thick, with alternating zones formed by nuclear cell bodies and their synaptic connections. Fig 2.2 shows a detailed schematic of cells comprising different layers of the retina. At the center of the retina is the optic disc also called the blind spot as it is devoid of photoreceptors. The retinal blood vessels that vascularize the retina and the nerve fibers that carry information to the brain converge at the optic disc. About 5mm from the optic disc is an avascular zone called the fovea, a region with highest density of cone photoreceptors. The innermost layer of the retina is the retinal pigment epithelium (RPE) rooted between the photoreceptor layer and the blood supply of the choroid. The RPE is comprised of a single layer of hexagonally packed cells containing pigment granules and plays a central role in retinal physiology. The human retina contains two types of photoreceptors- rods and cones. Their density varies as we move from the fovea to the periphery (Fig 2.3). The photoreceptor outer segments (OS) contain the light sensitive discs. The inner segments (IS) contain organelles where opsin molecules are formed and passed to the outer segments. The photoreceptor cell bodies constitute the outer nuclear layer (ONL). Their synaptic connection with the horizontal and the bipolar cells comprise the outer plexiform layer (OPL). The cell bodies of the horizontal, bipolar and amacrine cells lie in the inner nuclear layer (INL). The ganglion cell bodies in the ganglion cell layer (GCL) synapse with the bipolar and amacrine cells at the inner plexiform layer (IPL). The outermost nerve fiber layer (NFL) contains the axons of ganglion cells running in parallel towards the optic nerve which ultimately carries information to the central nervous system.

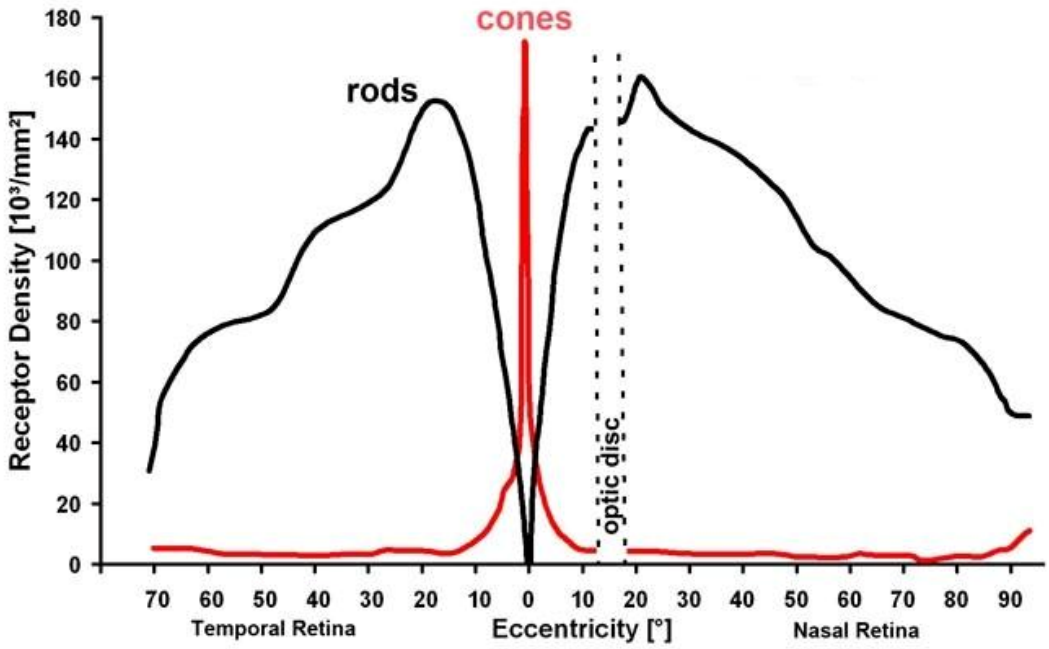

Figure 2.3: Photoreceptor density along the horizontal meridian (Image from http://webvision.med.utah.edu/)

2.2 Visual impairment and blindness

Visual impairment with increasing age is one of the major causes of functional disabilities in older American population (West, Munoz et al. 1997). Visual impairment may be defined as blindness (best vision of ≤ 20/200 in the better eye in the United States and 20/400 by the World Health Organization [WHO] definition) or low vision (<20/40 in the United States and <20/60 by WHO) (Congdon, Friedman et al. 2003). The 2000 US census estimated a total of 3.3 million Americans aged 40 years and older with visual impairment (Congdon, O'Colmain et al. 2004). With aging population, this number is increasing significantly along with eye-care costs (Ellwein and Urato 2002). The

morbidity resulting from blindness and low vision causes a huge socio-economic burden. For these reasons, early detection and treatment of eye diseases is especially important.

The three major diseases that affect the eye in American population today are age-related macular degeneration (AMD), glaucoma and diabetic retinopathy (Munoz, West et al. 2000). Glaucoma is a major cause of irreversible blindness worldwide and is characterized by damage to the optic nerve and resulting visual field loss. Glaucoma is generally caused by increase d intra-ocular pressure which can reduce the blood supply to the eye damaging the retinal neurons. Visual field loss starts out in the periphery and progresses towards the center. AMD is the leading cause of irreversible severe visual loss in older American population (Bressler, Bressler et al. 1988). It affects central vision associated with formation of drusen or neovascularization between the RPE and the choroid in the macula. Diabetic retinopathy, as the name suggests, is a side-effect of diabetes. Non-proliferative diabetic retinopathy is characterized by microaneurysms. In proliferative retinopathy, blood vessels proliferate and can hemorrhage, compromising vision. Diabetic retinopathy can lead to other complications like glaucoma, cataract and AMD. Despite advances in science, treatment of these diseases is successful only in a small percentage of cases. In many cases visual loss becomes apparent only after considerable damage has been done. Development of early diagnostic aids with the technology available at hand is one of the key factors in treatment of retinal diseases. Section 2.3 and 2.4 describes some of the technologies available for evaluating the health of the retina.

2.3 Optical Coherence Tomography (OCT)

Optical Coherence tomography (Huang, Swanson et al. 1991; Fercher, Hitzenberger et al. 1993) is a non-invasive imaging tool widely used in the management of retinal diseases. The high axial resolution makes OCT especially suitable for imaging of the stratified retina (Drexler 2007).Third-generation commercial OCT systems claim axial resolution of up to 2 micrometers.

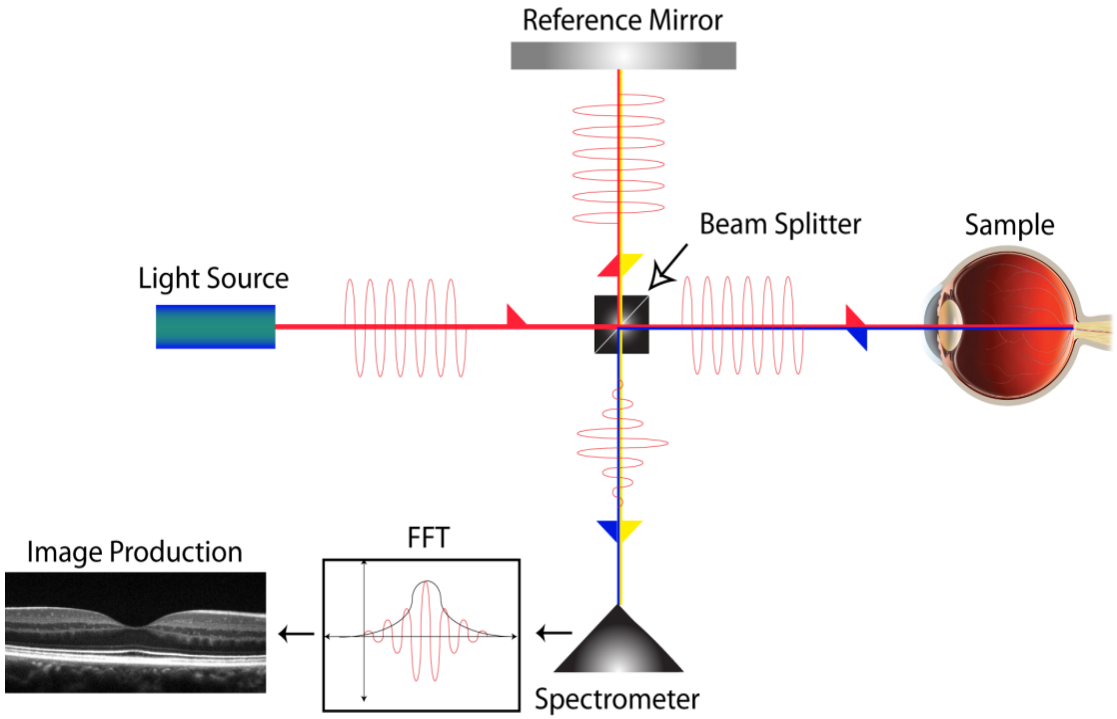

Figure 2.4: Schematic of the SD-OCT system. Light from the source is split at the beam splitter to enter the reference and the sample arms. Light reflected from the reference and the sample arms interfere and the modulated signal detected by the spectrometer. The signal is Fourier transformed to obtain the image of the retina.

OCT is based on the principle of interference of the light and can be described as an optical ultrasound. OCT measures the echo times delay and the magnitude of the back reflected light from the tissue being imaged (Wojtkowski 2010). The heart of an OCT

system is the Michelson interferometer. Light emitted from a low temporal coherence light source is divided by the beam splitter. One part of the light enters the reference arm which consists of a mirror and the other enters the sample arm which is the tissue being imaged. Light reflected from the reference arm and the sample interferes to produce a signal with constant amplitude. In order to obtain depth information the reference mirror is moved and a signal is obtained only when the interference between the two sources is constructive within the coherence time. This signal comprises one A-scan and a cross-sectional image can be obtained by either moving the sample or position of the scanning beam. The cross-sectional image is called a B-scan. This type of a system is called the time-domain OCT (TD-OCT) and was originally built in 1991.

Due to its inherent low acquisition speed, sensitivity and resolution, TD-OCT gave way to Fourier-domain (FD) or Spectral domain (SD) OCT technology (Geitzenauer, Hitzenberger et al. 2011). A schematic of the SD-OCT is shown in Fig 2.3. In a SD-OCT system the depth information from different locations of the sample is coded in the frequency spectrum of the modulated interference signal (Wojtkowski, Leitgeb et al. 2002; Cense, Nassif et al. 2004). The reference mirror remains fixed and the interference signal is detected by a spectrometer equipped with a high speed charge coupled device line scan camera. Since signals from different depths are measured simultaneously, there is dramatic increase in speed of acquisition and sensitivity as compared to TD-OCT. Using a raster scan imaging protocol, consecutive OCT images can be acquired at equally spaced intervals to obtain 3D OCT data (Wojtkowski, Srinivasan et al. 2005).

Axial resolution of a few micrometers is possible in OCT by using low coherence light. The axial resolution is solely dependent on the light source for a tissue being imaged. The axial resolution of an OCT system using light source with $\Delta\lambda$ as spectrum width (FWHM), λ as the center wavelength and η being the refractive index of the medium is given by

$$Resolution = \frac{2\ln 2}{\eta\pi}.\frac{\lambda^2}{\Delta\lambda}$$

The lateral resolution and depth of focus (DOF) in an OCT system are mutually dependent. Lateral resolution can be increased by increasing the effective numerical aperture of the system but it will decrease the DOF, which is inversely proportional to the square of the numerical aperture.

2.4 Retinal assessment

2.4.1 Fundus photography

Fundus photography is the most basic form of retinal examination performed for diagnosis of retinal diseases. It uses a low powered microscope attached with a camera specially designed to provide a detailed view of the fundus. Fundus photography can be performed under three modes of examination: color, red-free and angiography. Delori et al studied the effect of using narrow-band light source at various wavelengths on the visualization of the fundus (Delori, Gragoudas et al. 1977). They demonstrated increased contrast of various structures such as ILM, RPE, macula, optic disc, choroid under different spectral bands of illumination as compared to white light. Angiography technique involves photographing the retina by injecting fluorescent dyes. The dye

increases the contrast of the vasculature and enables detection of defects in the retinal circulation. Two angiographic methods used for examination of retina are sodium fluorescein angiography (abbreviated FA or FAG) and indocyanine green (abbreviated ICG) angiography.

Fundus photography techniques have been used in the diagnosis of various retinal diseases such as diabetic retinopathy (Lin, Blumenkranz et al. 2002), glaucoma (Hoyt, Frisen et al. 1973), macular degeneration (Holz, Bellman et al. 2001) and retinitis pigmentosa. Angiographic techniques have the risks of adverse effects on health caused due to injection of dyes (Jennings and Mathews 1994).

2.4.2 Retinal thickness analyzer

Retinal thickness analyzer (RTA) is a technique that was developed at Talia Technology Inc. (Neve Ilan, Israel) which was capable of rapidly obtaining retinal thickness map covering an area of 2mm x 2mm. It is based on the principle of projecting a narrow green laser slit beam obliquely on the retina and recording the backscattered light at an angle (Zeimer, Shahidi et al. 1996). The newer instrument is capable of obtaining scans of 3mm x 3mm and 6mm x 3mm with an axial resolution of 52µm and lateral resolution of 12µm. Asrani, Zou et al. (1999) designed a study using RTA to map normal retinal thickness at the posterior pole covering central 6mm x 6mm field of view. RTA has been used in the diagnosis of various diseases such as diabetic retinopathy (Fritsche, van der Heijde et al. 2002), AMD (Shahidi, Blair et al. 2002) and glaucoma (Tanito, Itai et al. 2004). In a study comparing RTA and OCT for assessing foveal thickness in eyes with macular diseases, it was found that in the presence of media opacities, OCT performs better than RTA.

2.5 Image Registration

Image registration is a technique in which two or more images taken with different sensors or at different times are aligned together. The purpose of image registration is to combine data in order to detect changes, enhance image quality or increase the information content. Image registration techniques are used in various fields today like medicine, computer vision, military surveillance and satellite systems (Goshtasby 2005).

With the rapid advent of new technologies such as X-rays, ultrasound, CT, MRI and OCT for imaging of the human body, the importance of image registration in medicine has increased considerably in the past few decades. The applications of image registration in medicine are manifold and include detection of anatomical and physiological changes over time, combining functional information with anatomy and comparing patient data with anatomical atlases (Hajnal, Hill et al. 2001).

In this work image registration was used to combine 2D retinal thickness data from the same patient at different but overlapping locations of the retina to create a larger mosaic. 3D volume images were also stitched to wide-field cross-sectional visualization. Such mosaics will aid in better visualization and detection of pathologies by comparing with data from normal subjects.

Typically an image registration algorithm will consist of the following steps:

1) Feature selection in which points of interest are manually or automatically selected.
2) Similarity measure which quantifies the degree of similarity between two images.
3) Transformation estimation in which a model is optimized to transform one image to align it to the other image which will give the best similarity measure.

4) Image transformation in which the image is transformed using the estimated model of transformation.

The feature selection step precedes feature based similarity measurement in which important features such as points, lines or regions are selected either manually or using some automated technique (Zitova, Flusser et al. 2005). Intensity based similarity measurement does not need feature selection as a prior step. The following few pages will briefly elucidate the similarity measures and transformation models that are commonly used in medical image registration.

2.5.1 Similarity measures

Similarity measures can be classified as either feature-based or intensity-based (Maintz and Viergever 1998).

2.5.1.1 Feature based registration

Feature based methods are used when invariant feature descriptors are present at all times between both the images. The following feature based methods are generally used for rigid body registration purposes but can be extended to non-rigid registration also. Techniques for non-rigid registrations like basis functions, splines, elastic registration and fluid registration are not discussed here. The most commonly used feature descriptors used in feature based registration is points and surfaces.

Point based registration involves identifying identical points describing the same feature on both the images, registering them and finding the transformation that will best fit them (Hajnal, Hill et al. 2001). The solution can be found by finding a least square fit.

Point based rigid body registration suffers from errors caused due to imperfect localization of points (Fitzpatrick, West et al. 1998).

Surface based registration is a commonly used technique in medical imaging. High contrast surfaces or boundaries can be automatically segmented from two images to register them using rigid body transformation by fitting the surfaces together (Hajnal, Hill et al. 2001). In the "*head and hat*" algorithm (Pelizzari, Chen et al. 1989) identical surfaces are identified in the images and the higher modality image is used as the reference surface (head). The surface to be registered (hat) is represented as a list of points. The hat surface is iteratively transformed with respect to the head surface by minimizing the square of distance between a point on the hat and the nearest point on the head in the direction of the centroid of the head (Hajnal, Hill et al. 2001). Another popular segmentation based method which uses distance transform is the *chamfer matching* technique using binary images for alignment (Borgefors 1984).

A versatile method called *Iterative closest point* (ICP) algorithm can work with point sets, curves, surfaces and volumes as landmarks (Besl and McKay 1992). The algorithm iteratively searches for the closest landmark points between two images and does a least square rigid body transformation to register the landmarks. This continues until a local minimum is reached matching the two surfaces.

2.5.1.2 Intensity based registration

Intensity based approaches are classically used for intra-modality image registration in which the image intensities are not expected to have changed very much between images. Such an approach has the advantage that it utilizes the information

content of the entire image and is not dependent on extraction of features. Intensity based measures can be used with 2D and 3D images alike.

When a linear relation exists between the images for cases like serially acquired MR images or images of the same subject taken at different times with the same scanner, *correlation coefficient* (CC) can be used as a similarity measure. In this measure, the corresponding image intensities are multiplied and the images are moved with respect to each other until the highest value for correlation is achieved. Formula for normalized cross-correlation is given by (Zitova, Flusser et al. 2005)

$$CC(i,j) = \frac{\sum_{(i,j)} \left(W_{(i,j)} - E\left(W_{(i,j)} \right) \right) \left(I_{(i,j)} - E\left(I_{(i,j)} \right) \right)}{\sqrt{\sum_{W_{(i,j)}} \left(W_{(i,j)} - E\left(W_{(i,j)} \right) \right)^2} \sqrt{\sum_{I_{(i,j)}} \left(I_{(i,j)} - E\left(I_{(i,j)} \right) \right)^2}}$$

where $E\left(W_{(i,j)} \right)$ is the mean pixel value of the image W and $E\left(I_{(i,j)} \right)$ is the mean pixel value of the image I.

One of the simplest similarity measures used for registering two images is to minimize the *sum of squared intensity differences* (SSD) between the images (Hajnal, Hill et al. 2001).

$$SSD = \frac{1}{N} \sum_{X_A \in \Omega_{\mathrm{A,B}}^{\mathrm{T}}} |A(X_A) - B^T(X_A)|^2$$

where X_A represent the pixel in image A , within an overlap domain $\Omega_{\mathrm{A,B}}^{\mathrm{T}}$ comprising N pixels. SSD can be normalized so it is invariant to the number of pixels in the overlap domain $\Omega_{\mathrm{A,B}}^{\mathrm{T}}$. SSD can be best utilized for images that differ only by Gaussian noise. Since the intensity differences are squared it is also very sensitive to a small number of pixels having large intensity differences between two images. *Sum of absolute differences* (SAD) will minimize the effect of such pixels (Hajnal, Hill et al. 2001).

$$SAD = \frac{1}{N} \sum_{X_A \in \Omega^{T}_{A,B}} |A(X_A) - B^T(X_A)|$$

Information theoretic techniques such as *joint entropy* and *mutual information* are based on probability theory. These techniques of registration minimize the amount of information in the combined image after registration. Such an approach can be used in multimodal registration such as MR, CT and PET images (Maes, Collignon et al. 1997).

A more robust form of correlation based similarity measure is computing correlation in the frequency domain. This technique is called the *Phase Correlation* (PC) measure which computes the cross-power spectrum of Fourier representation of the images and works well for frequency dependent noise. In this work the phase correlation technique has been utilized for registration of 3D retinal OCT volumes as detailed in the next chapter.

2.5.2 Transformation models

Image transformation maps the pixels in one image to the corresponding locations of pixels in the other image. The transformation models can be linear/rigid or elastic/non-rigid. Rigid body transformations include translation, rotation and scaling. Elastic transformations are more complex and are capable of locally warping the images. The mapping could take place from 2D space to 2D space, 3D space to 3D space or between 2D and 3D space. For the purpose of this work, we are interested in the first two types.

The simplest form of transformation is the *similarity* transform (Zitova, Flusser et al. 2005)

$$u = s\big(xcos(\varphi) - y\ sin(\varphi)\big) + t_x$$

$$v = s\big(xsin(\varphi) + y\ cos(\varphi)\big) + t_y$$

It consists of translations, rotations and scaling only and angles and curvatures are preserved. Such a transformation can be applied to rigid bony structures taken by scanners having little projection changes between scans.

Another linear model of transformation is called the *affine* transform in which straight lines remain straight and parallel line remain parallel but the lengths and angles may change. This is due to the shearing and scaling factor involved.

$$u = \ a_0 + a_1 x + a_2 y$$

$$v = \ b_0 + b_1 x + b_2 y$$

where a_0, a_1, a_2, b_0, b_1, b_2 are rotation, scaling, shearing and translation factors depending on their values. Affine transformations may be rough approximations for registrations where scanners are different or for inter-subject registrations in which the sizes of anatomical structures may differ.

In cases where the optical axis of the camera is not perpendicular to the structure being imaged, *perspective* or *homographic* model can be utilized. A quadrangle will be mapped onto a square and is satisfied by the equations (Zitova, Flusser et al. 2005)

$$u = \frac{a_0 + a_1 x + a_2 y}{1 + c_1 x + c_2 y}$$

$$v = \frac{b_0 + b_1 x + b_2 y}{1 + c_1 x + c_2 y}$$

For cases in which the above transformations do not satisfy higher order transformations may be derived from the landmark points that are selected. It is usually better to avoid higher order polynomials for medical imaging applications as it can unnecessarily warp the transformed image (Zitova, Flusser et al. 2005). The affine

transformation model was utilized for this work for montaging 2D thickness maps as described in the later chapter.

3. WIDE-FIELD THICKNESS MAP

Retinal thickness maps provide the value of thickness of the retina measured by taking the difference between the ILM and the RPE layers. Thickness analysis is an important means of identifying pathologies and studying their progression. Unfortunately for the purposes of image registration, the structural information present in the thickness maps is very low. Hence application of image registration methods directly on these maps is practically not possible. The only means for matching structures in order to align these maps is to either use the OCT scans or use the fundus images of the scans.

In this work we used the Line Scan Ophthalmoscope (LSO) fundus images of the OCT scans to find transformations for stitching the thickness maps together. Montaging was done using i2k Retina™ software (DualAlign LLC, Clifton Park, NY). Retinal vasculature and their cross over points are used as landmarks for registration. The software is propriety work that was derived and built on top of dual-bootstrap ICP algorithm developed by Yang et al. (Yang, Stewart et al. 2007).

3.1 Methods

3.1.1 Subjects

Normal subjects (n=20, males=14 and females=6) ranging from age 20 to 40 (mean = 26.7 years) were imaged on the left eye. Informed consent was obtained from after explanation of the nature and possible consequences of the study. All research on human subjects followed the tenets of the Declaration of Helsinki and was approved by Institutional Review Boards at the Medical College of Wisconsin, Children's Hospital of Wisconsin, and Marquette University.

3.1.2 Data acquisition

Subjects were imaged on the Cirrus ™ HD-OCT (Carl Zeiss Meditec, Dublin, CA) which has a theoretical axial resolution of 5µm and transverse resolution of 20µm. Sixteen overlapping volumes were obtained covering approximately 12mm x 14mm area of the retina centered on the fovea. Volumes were nominally 6mm x 6mm and consisted of 128 B-scans (512 A-scans/B-scan). Subjects were asked to focus on an internal fixation target comprising of a large green asterisk with red background during the scans which lasted for about 2.5 seconds each. Each volume scan had about 30 percent overlap with adjacent scans, and the scan pattern was derived via a combination of repositioning the system's scan region of interest and/or the internal fixation target.

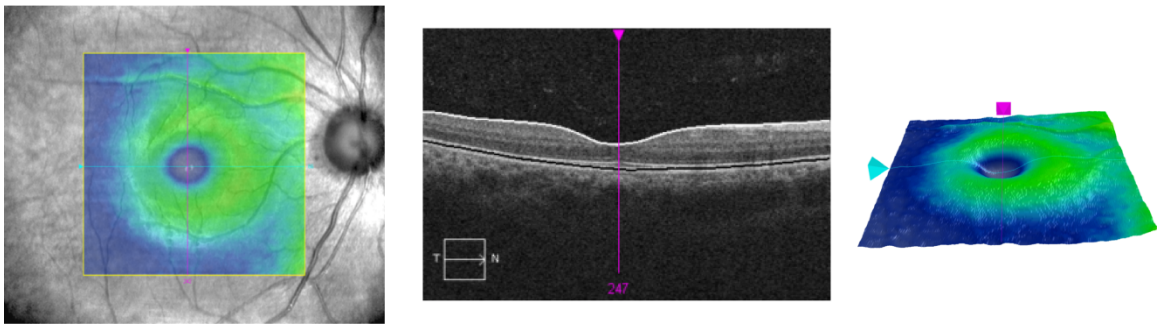

Figure 3.1: Cirrus HD-OCT macular cube scan protocol. LSO fundus image of the retina with overlaid thickness map showing the scan location (***Left***). B-scan through the center of the volume scan with ILM-RPE boundaries segmented (***Center***) Thickness value at each location is calculated by taking the difference between the ILM and RPE boundaries. Corresponding 3D view of the thickness map centered on the fovea (***Right***).

Retinal thickness was calculated using the built in Macular Analysis software on the Cirrus (software version 5.0), which is automatically determined by taking the difference between the ILM and RPE boundaries. The Line Scanning Ophthalmoscope (LSO) fundus images and the thickness map files for each location were exported from

the Cirrus Research browser software (version 5.0). The LSO fundus images were exported in TIF format and the thickness maps were exported as DAT files. The LSO images were cropped to the size of the scan as shown in Fig 3.2. The files were stored in a folder structure shown in Fig 3.3.

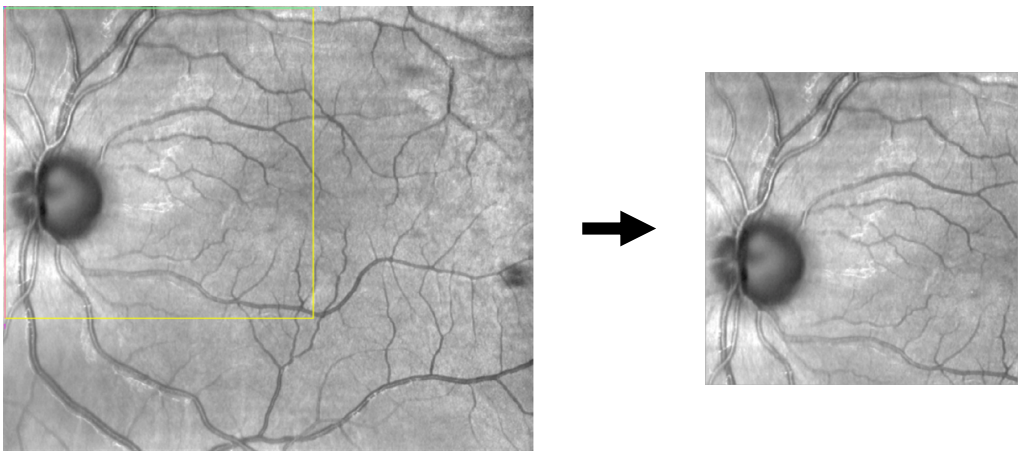

Figure 3.2: Cropping LSO fundus image to scanned area

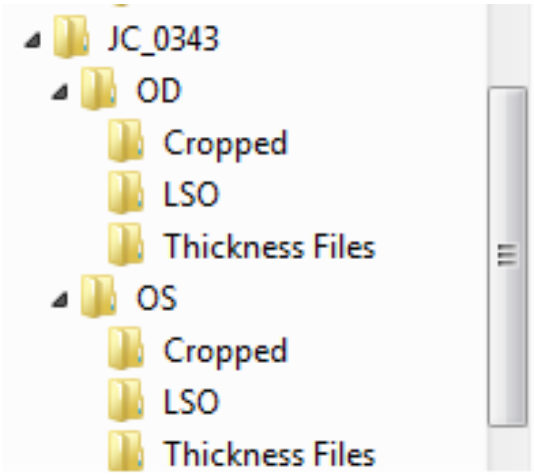

Figure 3.3: Folder structure for storing files for montaging process. The root folder is the subject number. Under the root folder are two folders *OD* and *OS* for the right and the left eye respectively. Under each of these folders are three sub-folders – *Cropped, LSO and Thickness Files*. The *LSO* folder contains the all the *LSO TIF* images exported from the Cirrus browser. The *Thickness Files* folder contains the corresponding thickness map *DAT* files. The *Cropped* folder contains the LSO files cropped to the size of the scan.

3.1.3 Montaging algorithm

The Cirrus LSO fundus image corresponding to each SD-OCT volume was cropped to the size of the scan and loaded into commercially available software i2k Align Retina (DualAlign LLC, Clifton Park, NY). The software provides various options to create a montage (Stewart 2009). Here the images were montaged using the affine transformation model. The i2k Align Retina software automatically saves the coefficients of the transforms applied to each image in a text file in a sequential order. Custom MATLAB software (Mathworks, Natick, MA) was developed to montage the thickness maps imported from cirrus research browser, according to the transforms that were applied to each thickness maps' corresponding fundus image. The transform coefficients were parsed and the coefficients were substituted in the affine transformation equations. The transformations were applied to the thickness maps after they were interpolated to the same size as the fundus images. The transformed maps were then stitched together using the montage coordinate system to create a wide-field thickness map.

In order to examine normal variation in these wide-field thickness maps, the thickness maps from different individuals were averaged. However, given the normal variability in axial length, the actual retinal area imaged for each subject varied. The 6mm x 6mm scan imaged by the OCT system is the nominal area based on the average axial length assumed by the system. For eyes with shorter axial length lesser area will be scanned, while more area will be scanned for eyes with longer axial length. The final stitched maps had to be corrected for inter-individual differences in axial lengths. Axial length of each eye was measured using Zeiss IOL Master (Carl Zeiss Meditec, Dublin, CA). Subjects' axial lengths ranged from 21.99 to 26.24mm. We corrected the later scale of each wide-field thickness map by simply adjusting the image scale by the ratio of each

subject's axial length to that assumed by the system (24.46mm). Also eyes with longer axial lengths have more curved retina which makes it difficult to image the peripheral locations using OCT. This limits the amount of area that can be imaged. The microns/pixel resolution was calculated from the actual scan length and was used to crop a rectangular 12mm x 14mm area of individual montaged thickness maps. This total usable area was determined based on the smallest axial length and segmentation errors in the peripheral regions. The rectangle was centered on the fovea by manually selecting a point close to the fovea and letting the program search for the lowest value of thickness about 1mm diameter around that point. This allowed the thickness maps to be lined up about the fovea. The aligned maps were interpolated to have the same size as the median of sizes of all the maps and averaged pixel-wise to create a normative thickness map. A pixel-wise standard deviation map was also calculated.

3.2 Results

Different options are available for transformation models in the i2k Retina software. A qualitative analysis was performed for different transformation models available to find out which transformation model best suited our application. Fig 3.4 shows the final montaged LSO maps for four transformation models – reposition (translation), affine, homography with radial distortion (HWR) and quadratic. The images are scaled according to their actual size. Due to the curved shaped of the retina, reposition alone cannot montage the images correctly and some vessel misalignments will always be present. A simple reposition transform (Fig 3.4A) is applied to show the approximate size of the final montage. The vessel misalignments are circled red. Fig 3.4B is a result of montage using the affine transformation model. The size of the map is approximately

equal to that in Fig 3.4A. With HWR model there is significant distortion at the corners caused by shearing and scaling (Fig 3.4C). For quadratic model the distortion is seen as squeezed image on the right edge (Fig 3.4D). Similar results were found on other subjects. Although HWR and quadratic transformations technically montage the images without any misalignments, for our purpose we choose the affine transformation as it maintains the integrity of the thickness maps by causing lesser distortion.

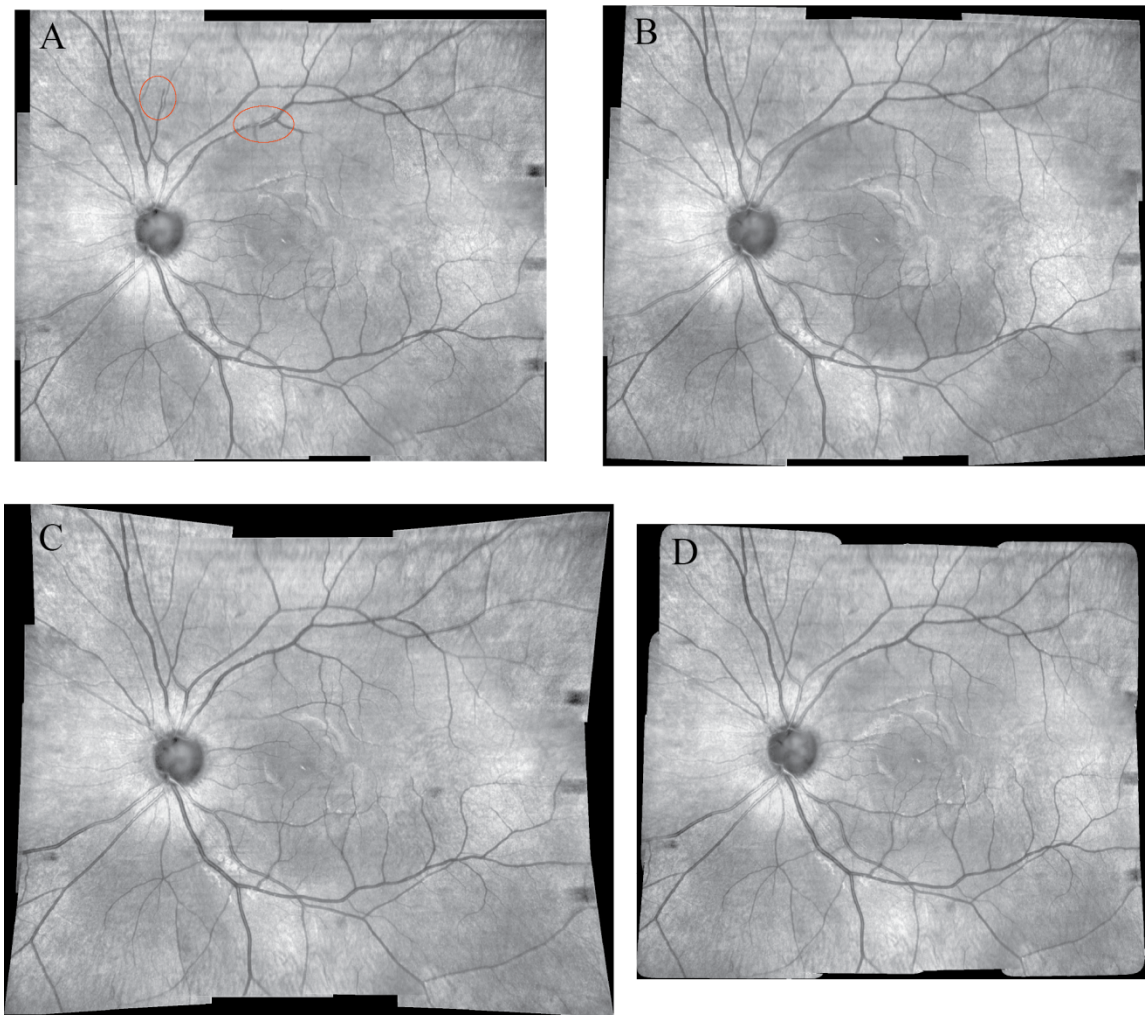

Figure 3.4: Montage of LSO images using four different transformation models from i2k Retina software. Result of montaging using Reposition (***A***), Affine (***B***), Homography with Radial Distortion (***C***) and Quadratic (***D***) transformation.

Fig 3.5 shows the layout of the GUI developed for montaging the thickness maps. The thickness map is in the raw form where segmentation errors are visible in the lower left corner. The *Select Name* button allows the user to navigate to the patient directory. The *Crop* button on the left hand side allows the user to select LSO images to crop to the scan size. The *Montage* button is linked to i2k Align Retina software (DualAlign LLC, Clifton Park, NY) through an API, which allows automatic montaging of the cropped LSO images. On clicking the *Display* the thickness maps are montaged and the result is displayed in the right hand panel. The left panel displays the LSO montage. If the *Point* radio button is selected, clicking anywhere on the LSO montage will show the thickness at that point on the thickness map. If the *Line* radio button is selected, a line drawn on the LSO montage will display a profile of the thickness through that line, on the lower panel as seen in Fig 3.5.

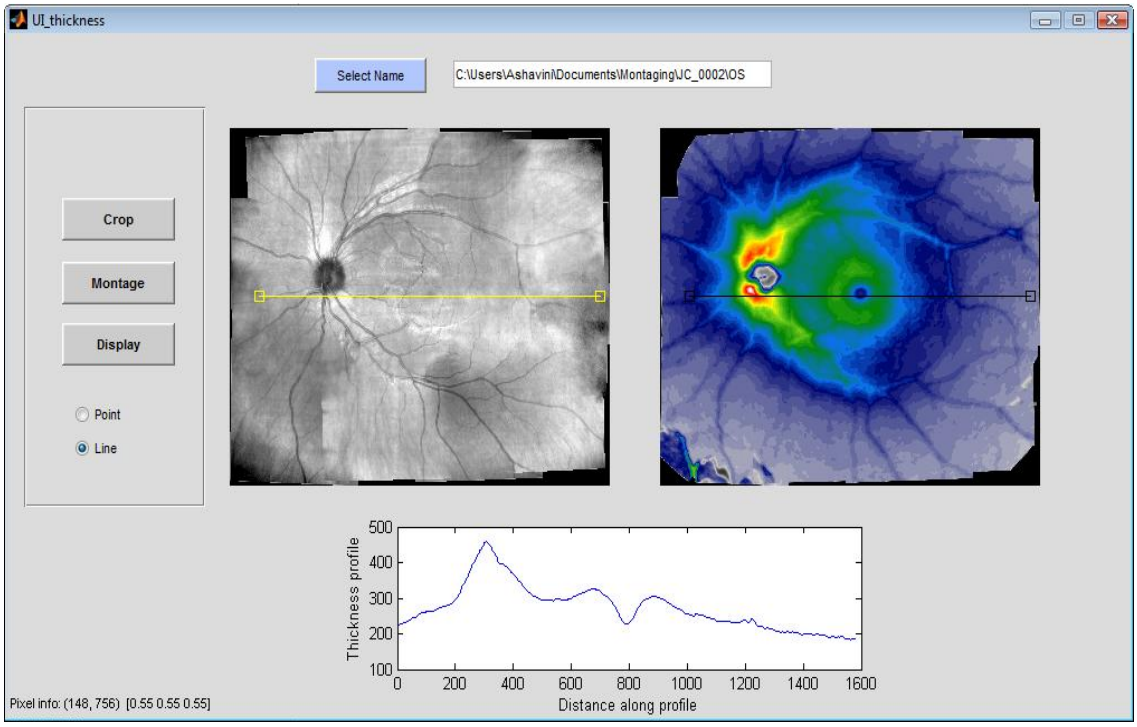

Figure 3.5: GUI displaying montaging results.

The final cropped LSO montage and the corresponding thickness map montage for a single subject is shown in Fig 3.6. The 12mm x 14mm montage is large enough to include the entire foveal pit and the optic disc. The montaging algorithm was successfully applied on all twenty eyes.

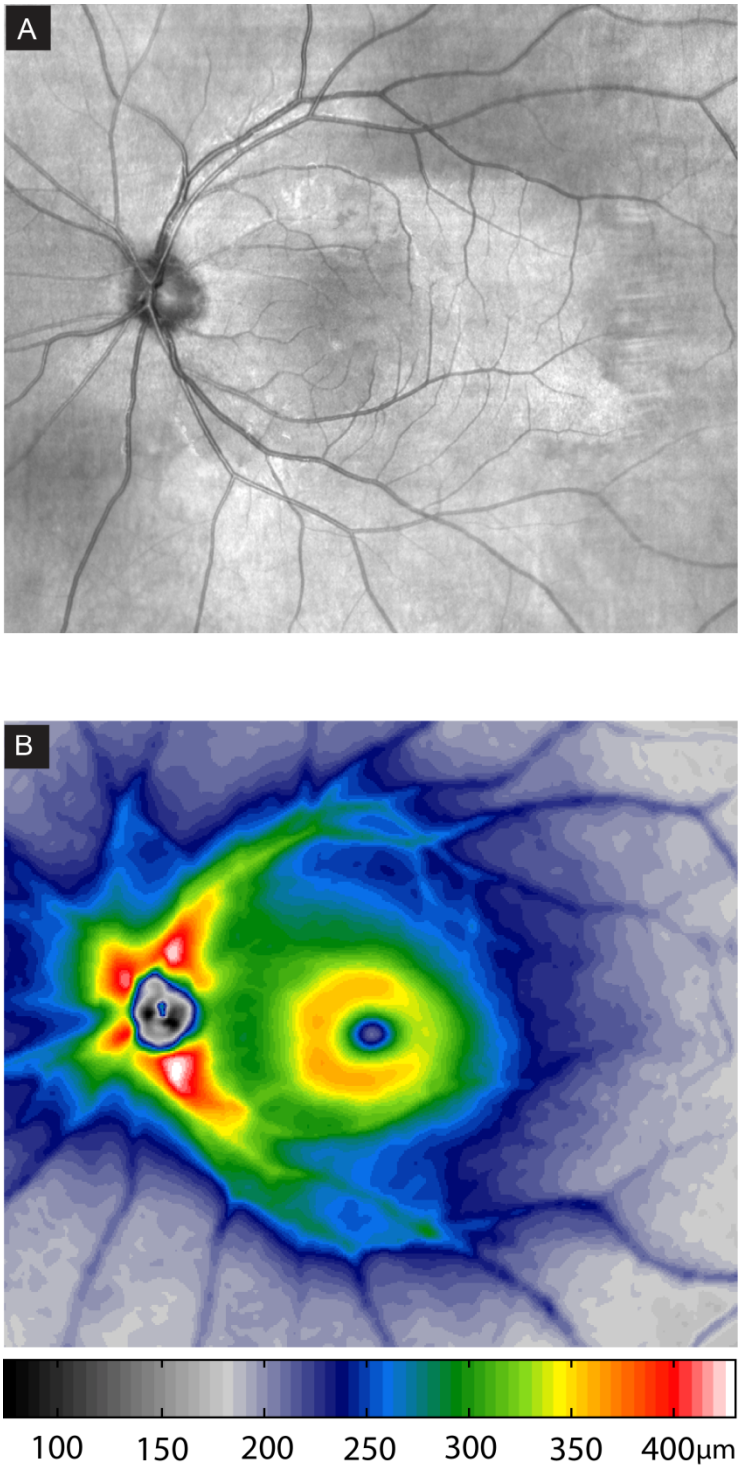

Figure 3.6: Montaged wide-field fundus and thickness map. i2k Retina program was used to montage sixteen 6mm x 6mm LSO images using affine transformation model (***A***). Corresponding transformation equations were used to montage the thickness maps (***B***). The final map is 12mm x 14mm centered on the fovea.

The area covered by sixteen overlapping 6mm x 6mm OCT volumes is theoretically much larger than 12mm x 14mm. But for an eye with shorter axial length the effective area scanned decreases in proportion to the ratio of subjects axial length to the one assumed by the system. The effective overlap area will also decrease which could affect registration. Hence larger overlaps were used with significant redundancy in sampling. Also for longer axial lengths (myopic eyes), the curvature of the eye causes the OCT scans to fall beyond the scanning area. Fig 3.7 shows wide-field thickness maps from five different individuals. There is a clear variation in thickness in the central macular regions between individuals. The difference in thickness is lesser towards the periphery. To quantify the inter-subject variability, we computed the average wide-field retinal thickness and the standard deviation in retinal thickness across the 20 subjects. The final normative average and standard deviation thickness maps are seen in Fig 3.8. The typical morphology of the optic nerve head and the foveal pit are visible in the average thickness map. As seen from the standard deviation map, there was substantial variation in thickness a values in the wide-field maps. Again we can see that the standard deviation is larger at the macula and the vessel arcade. The standard deviation is extremely high at the ONH since the maps were not aligned to the optic nerve. We examined three, 3mm-diameter, regions of interest (ROI) – one centered on the optic disc, one centered on the foveal pit, and one located 5.6mm temporal to the fovea. The average standard deviation in these regions was 58.5μm, 21.85μm, and 10.4μm, respectively.

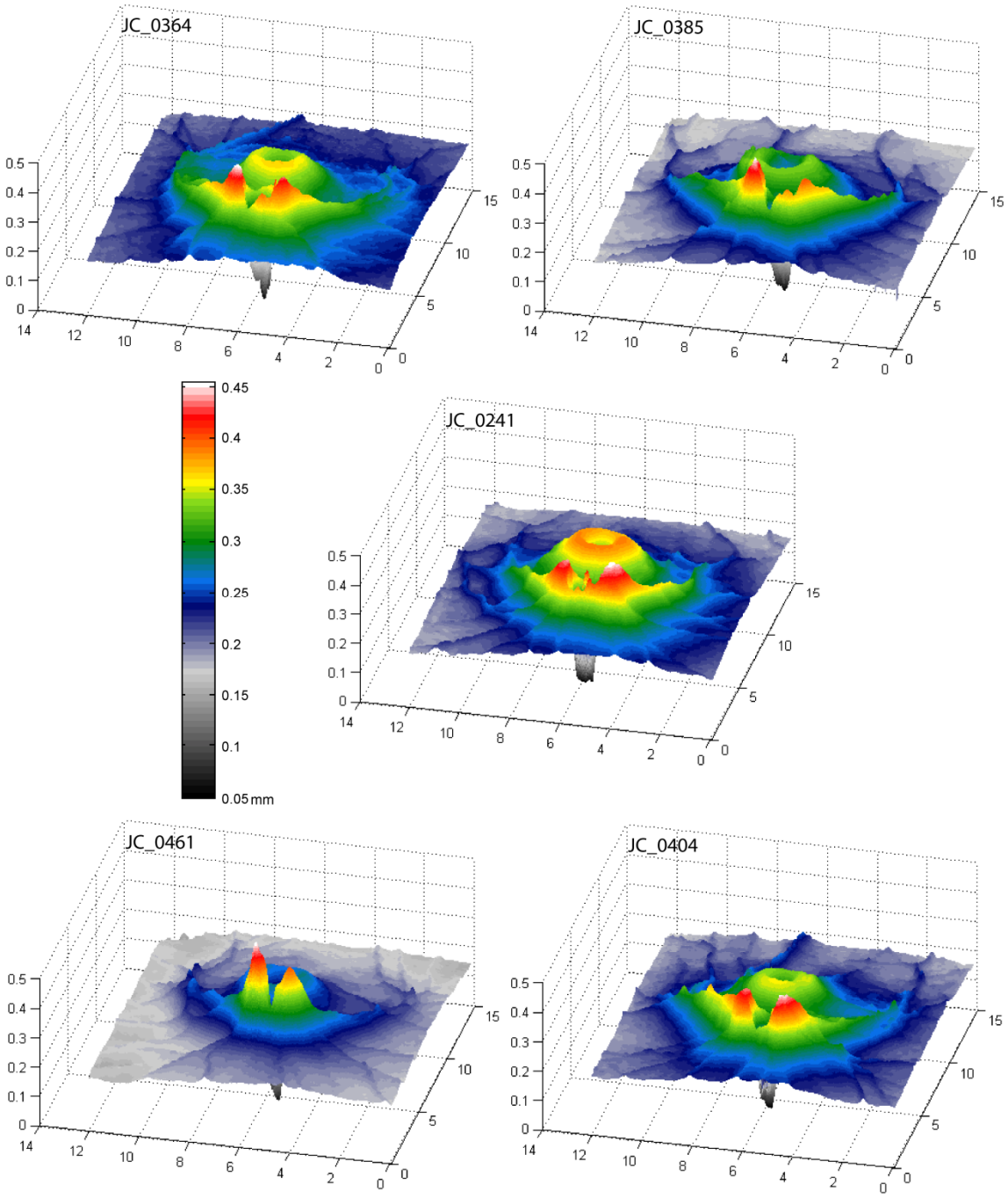

Figure 3.7: Wide-field thickness maps from five normal eyes. All dimensions are in mms. A large variation in thickness is clearly seen in the central macular region. The variation is lesser towards the periphery.

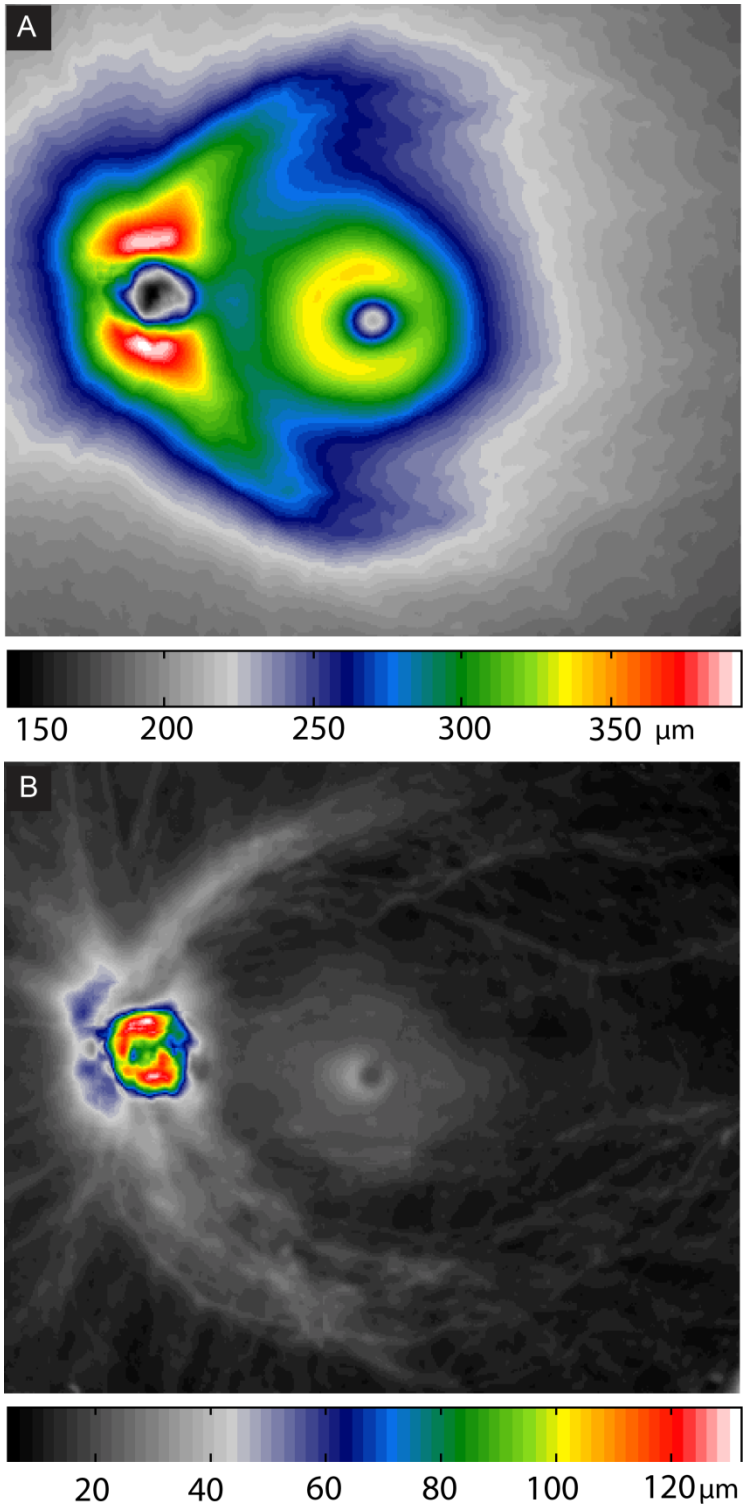

Figure 3.8: Normative wide-field thickness and standard deviation maps. Thickness maps from twenty normal individuals were averaged to create a 12mm x 14mm normative wide-field thickness map (***A***). Standard deviation map (***B***) of 12mm x 14mm was calculated to show the differences in thickness values among normals.

4. REGISTRATION AND STITCHING OF RETINAL OCT VOLUME SCANS

OCT volume scans are important for visualization of diseases such as Diabetic macular edema and glaucoma. Considering the acquisition speeds of current OCT systems, OCT volume scans are restricted to 6mm x 6mm area of the retina to prevent errors that can be caused due to subject's eye motion. Wide-field OCT volume view covering the fovea as well as ONH regions will be useful in better diagnosis of diseases. In this work a 3D image registration algorithm customized for creating large field-of-view (FOV) Optical Coherence Tomographic volumes was developed. Overlapping retinal volumes obtained using SD-OCT system were registered and stitched together to create a continuous larger volume view of the retina. The algorithm essentially involves two steps: 3-D Phase-Correlation and 2-D Pseudo-Polar Fourier transform.

The Phase Correlation measure (Kuglin and Hines 1975) is Fourier domain intensity based technique that computes the cross-power spectrum of Fourier representation of images. This technique has been robust in estimating large translations and rotations (Reddy and Chatterji 1996) and has been extended to sub-pixel accuracy (Foroosh, Zerubia et al. 2002).

Typically, rotation can be recovered using Fourier transform in polar or log polar domain where rotations will be reduced to translations. Direct computation of polar Fourier transform is computationally expensive. Other techniques for computing polar Fourier transform involve interpolation of 2-D DFT to polar coordinates in the Fourier domain (Reddy and Chatterji 1996; Wolberg and Zokai 2000). But these approaches are prone to errors due to discretization of Fourier transforms on polar or log-polar grids.

Averbuch et al. developed a technique called pseudo-polar Fourier transform (PPFT) which enables evaluation of fast Fourier transform on non-Cartesian grids (Averbuch, Coifman et al. 2006). This technique was shown to be useful in estimating large rigid-body motions (Keller, Averbuch et al. 2005) and registration of 3-D volumes (Keller, Averbuch et al. 2005; Keller, Shkolnisky et al. 2006). Chou et al. developed a generalized version of the PPFT and demonstrated its use in registering 2-D SD-OCT images (Chou, Izatt et al. 2009).

To find global translation between two volume-scan sets, 3D Phase Correlation method is used. This was inspired by the 3D stitching plugin available in Fiji (Preibisch, Saalfeld et al. 2009), an open source ImageJ (Abramoff, Magelhaes et al. 2004) distribution. Phase correlation is a Fourier domain technique which allows fast and accurate estimation of large translations by taking advantage of fast Fourier transform (FFT) which is particularly suitable for stitching large volume files with large relative displacements. Also phase correlation method is less affected by noise than most spatial domain techniques and hence this method was selected for registration of OCT images which are affected by speckle noise. Once the volumes are registered relative to each other, a 2-D pseudo-polar Fourier transform (PPFT) technique is used to find rotational motion between overlapping slices in the registered set. Computation of PPFT requires only 1D-FFTs and the algorithm does not require any re-gridding or interpolation. This rotational motion between the overlapping slices could be caused due to lateral eye motion and due to change in angle of the imaging scanner.

4.1 Methods

4.1.1 Image Acquisition

Data collected using the thickness mapping protocol was used here. Only the B-scan movie files were needed for this algorithm. The data was imported to Cirrus Research browser and the B-scan OCT movies were exported as 8-bit TIF files to be used as input files for the algorithm. Additional data was collected on one subject on the Bioptigen SD-OCT (Bioptigen, Inc., Research Triangle Park, NC) and Spectralis SD-OCT (Heidelberg Engineering, Inc, Heidelberg, Germany). Similar protocol was used as the Cirrus HD-OCT and four overlapping volume scans were obtained covering approximately 10mm x 10mm region around the fovea.

4.1.2 Registration and stitching algorithm

4.1.2.1 Phase Correlation

The Phase Correlation Method was used for global 3D alignment of a pair of overlapping OCT volume scans. Phase Correlation is a Fourier tansform based technique that can be used to calculate translational offset between two images. The inverse Fourier transform of the phase correlation function between two images shifted relative to each other gives information about the shift (Δx, Δy, Δz). Let $I_1$and I_2 be two volumes that differ only by translational shift i.e,

$$I_2(x, y, z) = I_1(x - \Delta x, y - \Delta y, z - \Delta z)$$

Their Fourier transforms F_1 and F_2 will be related by

$$F_2(\vec{w}) = F_1(\vec{w}) * e^{-j2\pi(w_x \Delta x, w_y \Delta y, w_z \Delta z)}$$

where w_x, w_y and w_z are points at which the samples are calculated in the Fourier domain. By taking the inverse FFT of the cross-power spectrum, the translation parameters (Δx, Δy, Δz) can be estimated from the delta function

$$F^{-1}\left(\frac{F_1 F_2^*}{|F_1 F_2^*|}\right) = F^{-1}\left(e^{j2\pi(w_x \Delta x, w_y \Delta y, w_z \Delta z)}\right) = \delta(x - \Delta x, y - \Delta y, z - \Delta z)$$

Due to periodicity of Fourier transforms eight different possible translations in 3D need to be evaluated by means of cross-correlation on the overlapping area of the images (Preibisch, Saalfeld et al. 2009). The translation with highest cross-correlation is selected.

4.1.2.2 2-D Pseudo-polar Fourier transform

Once the global translations are found for aligning the volumes, each overlapping pair of B-scans is considered separately to find the angle of rotation between the B-scan pair. Rotation in only x-y plane is considered. It is assumed that there is no rotation in the z-plane. The rotation angle between each pair of B-scans is independent of others.

The 2D Fourier transform of an image I of size NxN on Cartesian grid (k, l) and M=2N+1 is given by

$$\hat{I}(k,l) = \sum_{u=-\frac{N}{2}}^{\frac{N}{2}-1} \sum_{v=-\frac{N}{2}}^{\frac{N}{2}-1} I(u,v) e^{-\frac{2\pi i(uk+vl)}{M}}, \quad k, l = -\frac{M}{2}, \ldots, \frac{M}{2} - 1 \qquad (1)$$

The following explanation about evaluation of pseudo-polar Fourier transform has been described in (Keller, Shkolnisky et al. 2005). The pseudo-polar grid is an approximation of the polar grid. The pseudo-polar Fourier transform (PPFT) evaluates the 2D Fourier transform of an image on the pseudo-polar grid given by the combination of a pair of sectors

$$P \triangleq P_1 \cup P_2$$

Where

$$P_1 \triangleq \left\{\left(-\frac{2l}{N}k, k\right) \middle| -\frac{N}{2} \leq l \leq \frac{N}{2}, -N \leq k \leq N\right\}$$

$$P_2 \triangleq \left\{\left(k, -\frac{2l}{N}k\right) \middle| -\frac{N}{2} \leq l \leq \frac{N}{2}, -N \leq k \leq N\right\}$$

The sets P_1 and P_2 and the pseudo-polar grid P are shown in Fig 4.1.

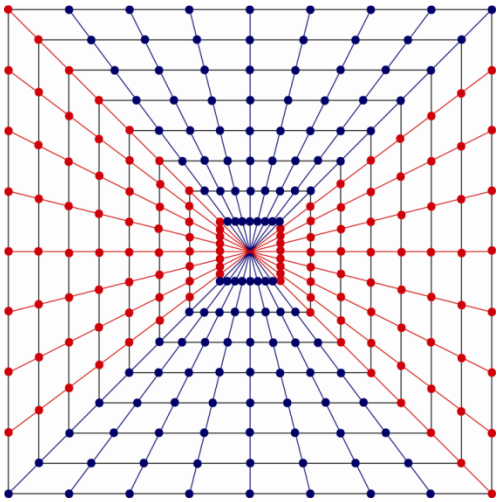

Figure 4.1: Pseudo-polar grid P comprising of sectors P_1 and P_2. The blue radial lines make the vertical sector P_1 and the red radial lines make the horizontal sector P_2 .

Sampling the Fourier transform of image I given by Eq. (1) on the pseudo-polar grid P, we obtain the pseudo-polar Fourier transform, which is defined for $k = -N, \ldots, N$ and $l = -N/2, \ldots, N/2$, as

$$\hat{I}^1_{PP}(k,l) \triangleq \hat{I}\left(-\frac{2l}{N}k, k\right) = \sum_{u=-\frac{N}{2}}^{\frac{N}{2}-1} \sum_{v=-\frac{N}{2}}^{\frac{N}{2}-1} I(u,v) e^{-\frac{2\pi i}{M}\left(-\frac{2l}{N}ku+kv\right)} \qquad (2a)$$

$$\hat{I}_{PP}^{2}(k,l) \triangleq \hat{I}\left(k, -\frac{2l}{N}k\right) = \sum_{u=-\frac{N}{2}}^{\frac{N}{2}-1} \sum_{v=-\frac{N}{2}}^{\frac{N}{2}-1} I(u,v) e^{-\frac{2\pi i}{M}\left(ku - \frac{2l}{N}kv\right)} \qquad (2b)$$

The resolution of the pseudo-polar grid is N + 1 in the angular direction and M = 2N + 1 in the radial direction. As can be seen in the Fig 4.1, the points are equally spaced along the rays and the rays are spaced at constant slopes. The vertical sector P_1 given by Eq. (2a) and the horizontal sector P_2 given by Eq. (2b) are calculated separately and then combined to form the full pseudo-polar grid. The resampling of $\hat{I}$ on the pseudo-polar grid is achieved by the fractional Fourier transform (FRFT) (Bailey and Swarztrauber 1991). For a given vector X, of length N, the FRFT is defined as

$$(F^{\alpha}X)(l) = \sum_{u=-\frac{N}{2}}^{\frac{N}{2}-1} X(u) e^{-\frac{2\pi i \alpha l u}{N}}, \quad l = -\frac{N}{2}, \ldots, \frac{N}{2} \qquad (3a)$$

For α=1 we get ordinary 1D FFT and for α=-1 we get ordinary 1D IFFT. For a detailed explanation on how FRFT is calculated, the above equation can be re-written as

$$(F^{\alpha}X)(l) = \sum_{u=-\frac{N}{2}}^{\frac{N}{2}-1} X(u) e^{\frac{\{-i\pi[-(u-l)^2+u^2+l^2]\alpha\}}{N}} \qquad (3b)$$

$$(F^{\alpha}X)(l) = e^{-\frac{i\pi l^2 \alpha}{N}} \sum_{u=-\frac{N}{2}}^{\frac{N}{2}-1} \left(X(u) e^{-\frac{i\pi u^2 \alpha}{N}}\right) . e^{\frac{i\pi (l-u)^2 \alpha}{N}} \qquad (3c)$$

The terms inside the summation can be calculated as a convolution of two sequences. The output of the convolution is multiplied by a phase factor outside the summation term.

The PPFT $\hat{I}_{PP}^{1}$ can be computed by applying a 2D Fourier transform to each column of I and then applying the FRFT to each row with $\alpha = 2k/n$, where k is the index of the row. The PPFT $\hat{I}_{PP}^{2}$ is computed on similar lines except the rows and columns are switched. The complexity of 2D pseudo polar Fourier transform is $25N^2 \log N$ which is proportional to Cartesian 2D FFT with a complexity of $10N^2 \log N$.

Rotations between a pair of images are reduced to translations in the polar domain. Once the PPFT is computed for a pair of B-scans, the angle of rotation between the pair is found by applying phase-correlation. Any local translation between the pair resulting from rotation is calculated using normalized cross-correlation.

4.1.2.3 Feathering or center-weighting image blending

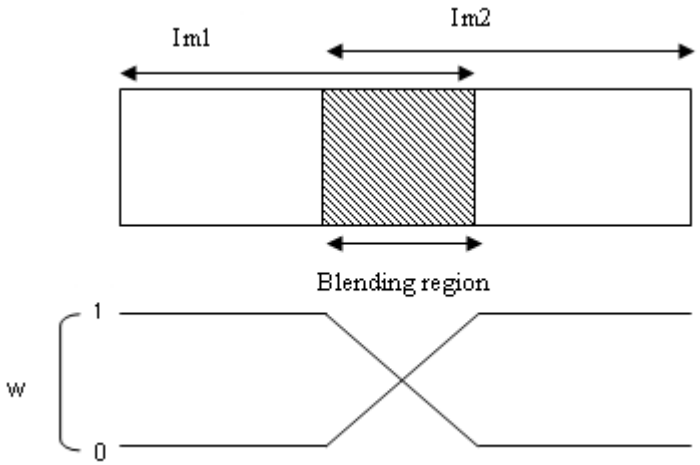

Figure 4.2: Illustration of feathered image blending technique.

Finally the B-scan pairs are stitched together using feathering or center weighting image blending (Szeliski 2006). In this simple approach, the pixel values in the blended regions are weighted average form the two overlapping images. Fig 4.2 illustrates feathered blending where *w* is the weighting factor. Fig 4.3 shows the overall flow-chart of all the steps involved in stitching two volumes together. The resulting volume is saved in the computer memory at the specified location. This volume can be used again as input for another run of the algorithm to stitch another overlapping volume, subsequently creating a bigger montage. The algorithm was implemented in MATLAB 7.10.0 and Parallel Computing toolbox was used for finding the rotation angles for faster processing on multi-core CPUs.

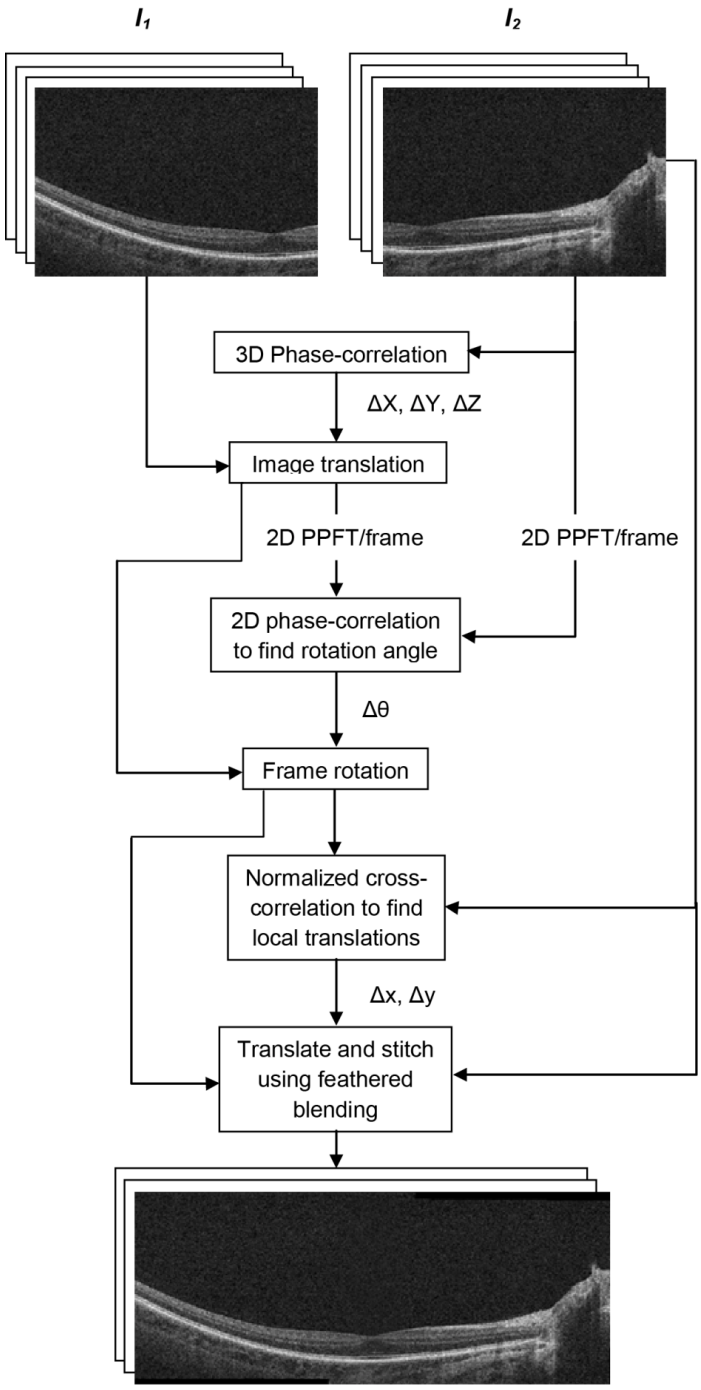

Figure 4.3: Flow-chart for steps involved in the volume stitching algorithm.

4.2 Results

While wide-field thickness maps have utility to monitor global changes in retinal thickness, visualization of large field-of-view B-scans would be helpful for examining retinal pathology on a local level. Most SD-OCT systems are restricted in their ability to acquire retinal volumes larger than 6mm x 6mm; and even for those that can acquire larger volumes, the sampling density needs to be decreased in order to keep the acquisition time low. We acquired two overlapping volumes, each one having moderately high sampling density and covering a nominal 6mm x 6mm retinal area. The volumes were stitched together using the volume stitching method. The volume stitching algorithm was successfully applied to stitch volumes from multiple SD-OCT systems (Spectralis, Bioptigen, Cirrus), acquired on a single subject using protocols specified in Table 1. Due to memory limitations of the system on which Matlab was running, the system frequently ran into 'out of memory' errors in Matlab. Hence, the higher resolution volumes from Bioptigen and Heidelberg were scaled down to 50% of their size. However, this problem can be avoided by running Matlab on 64 bit operating systems.

Due to change in imaging angle and subject's head and eye motion, global alignment alone cannot correct for misalignments between individual frames of the two overlapping volumes (Fig 4.4). Frame 1 of the stitched volume is correctly aligned (Fig 4.4A) whereas frame 90 is not (Fig 4.4B). After finding local rotation and translation all the frames are aligned (Fig 4.4C, D). Retinal thickness of a single 6mm B-scan was compared with a scan obtained by stitching two overlapping B-scans (Fig 4.5). The scans were manually segmented to obtain the retinal thickness (Fig 4.5 C). The thicknesses obtained using the two methods vary slightly in some areas. This could be attributed to

error occurring due to manual segmentation, change in eye shape when looking in different directions and errors due to change in target fixation location.

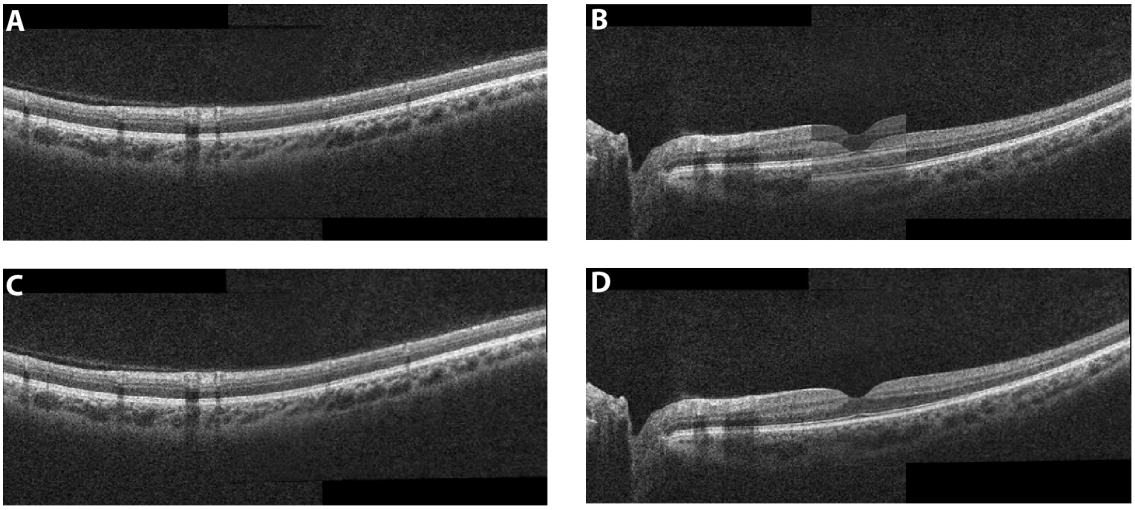

Figure 4.4: Illustration of global and local alignment. Top images (A & B) are frames 1 and 90 from a stitched volume aligned using 3D phase correlation. Bottom images (C & D) are the same frames 1 and 90 after applying 2D PPFT for individual frame wise rotational and translational alignment

Fig 4.5 shows the results of stitching two sub- volumes from Spectralis SD-OCT. The fundus scan shows the area of the stitched volume. The line drawn through the fundus through the fovea corresponds to the location of the scan on the right. The axial length of the eye used in this scan was 24.86mm. The size of the stitched B-scan is 8.78mm corresponding to the total size of the volume which is 5.91mm x 8.78mm. Similar results were obtained on the volumes taken on Bioptigen and Cirrus SD-OCTs (Fig 4.6, 4.7) along with their SVPs. The SVP is obtained by summing the pixels in the volume along the y-plane.

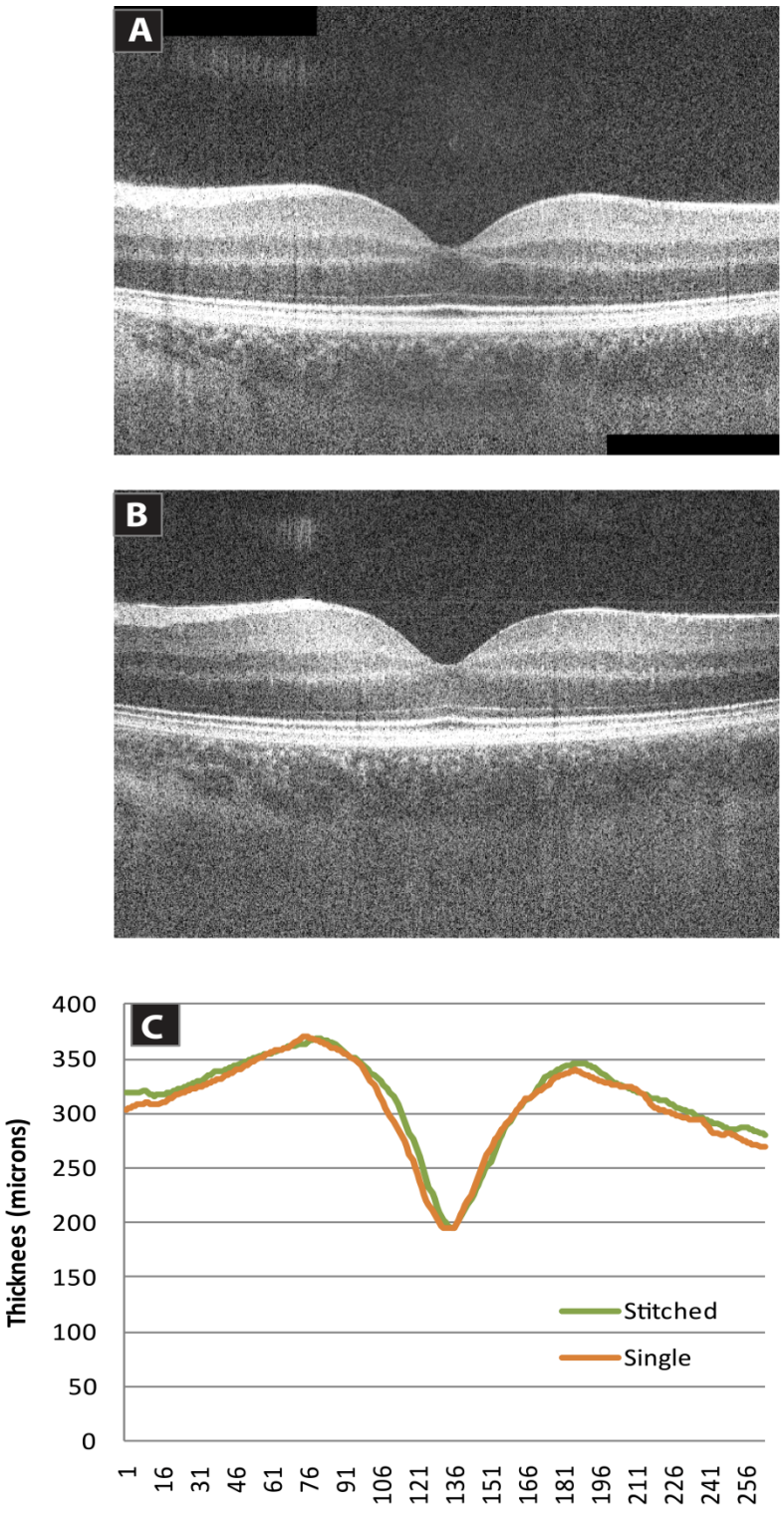

Figure 4.5: Comparison of retinal thickness of a single B-scan. Two overlapping B-scans stitched together (A) and a single scan (B) covering the same area were segmented manually to obtain their thickness plots (C).

Table 2 summarizes the time taken for stitching of two overlapping volumes. The time required for registration of volumes depends only on the size of the volumes for finding the phase correlation and the overlapping area to find the PPFT. As seen in from the examples in the table there is direct correlation between the size of the volumes and time taken for stitching. The size of single volumes acquired on different instruments differs based on the model eye size assumed by the system. The final size of the stitched volume depends on the overlap between the volumes and the corrected size of individual volumes.

Instrument	Area (mm) (corrected for axial length)	Number of B-scans	Space between scans (µm)	A-scans/B-scan	A-scans/sec	Axial Resolution (µm)
Bioptigen	6.2 x 6.2	128	48.4	512	37,000	2
Cirrus	6.1 x 6.1	128	47.6	512	27,000	5
Spectralis	5.9 x 5.9	97	60.9	1024	40,000	3.9

Table 1. Specifications for different instruments.

Instrument	**Size in pixels (of individual volumes)**	**Time (secs)**	**Area (mm) (corrected for axial length)**
Bioptigen	320x240x128	124	6.1 x 10.4
Cirrus	300x200x128	80	6.2 x 9.9
Spectralis	503x170x97	122	5.9 x 8.8

Table 2. Time taken for stitching.

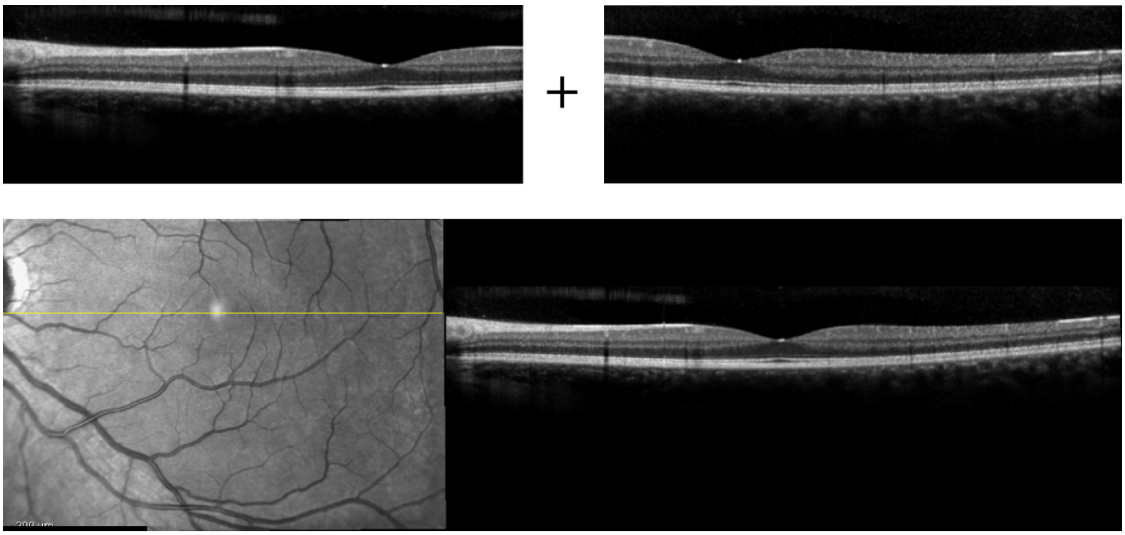

Figure 4.6: Volume stitching of two sub-volumes taken on Spectralis SD-OCT

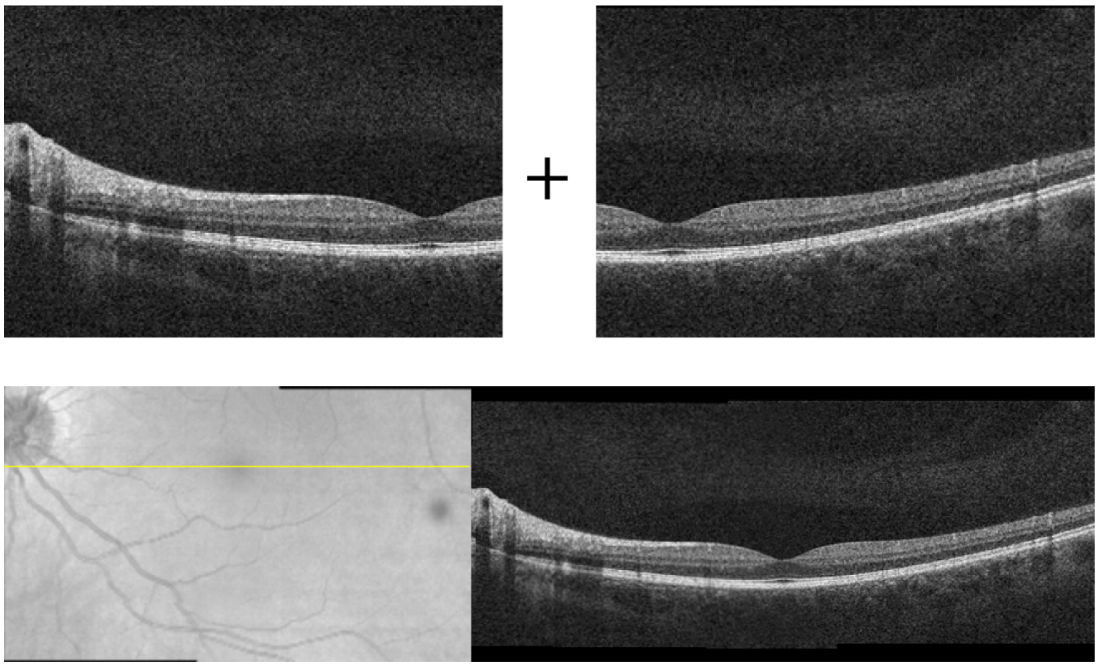

Figure 4.7: Volume stitching of two sub-volumes taken on Cirrus HD-OCT.

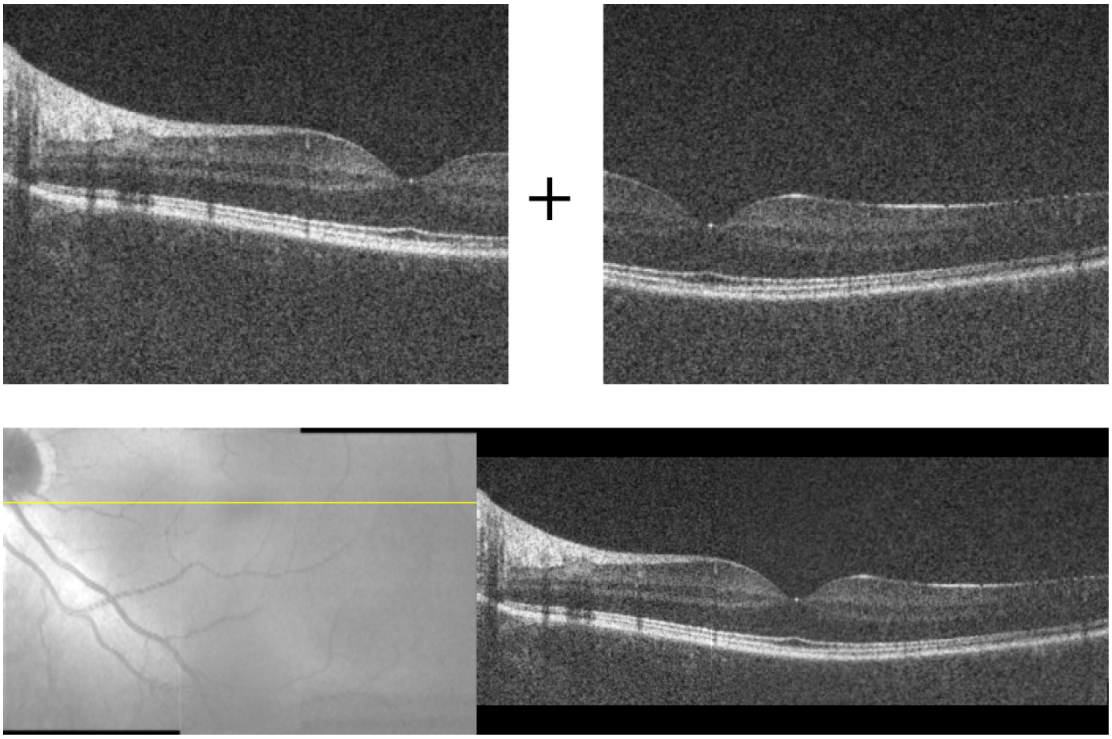

Figure 4.8: Volume stitching of two sub-volumes taken on Bioptigen SD-OCT.

5. SUMMARY, DISCUSSION & CONCLUSION

The objective of this work was to develop tools for creating wide-field views of the retinal thickness maps and OCT volume scans. Another aim was also to start establishing a normative wide-field thickness map database. The montaging of overlapping thickness maps was done by using transformations available from i2kRetina™ software. Rigid-body parameters for stitching of OCT volume scans were found by using phase-correlation and PPFT methods. In the following paragraphs we discuss the results and limitations of the methods and provide some future directions.

5.1 Wide-field Thickness maps

We developed an offline method for creating wide-field thickness maps of the retina. The method could be applied to any SD-OCT system, with the requirement that the raw retinal thickness data be available and good quality fundus or LSO/SLO images are available across the area being scanned. One advantage of our approach is that each volume is acquired with a sampling density that provides enough resolution to accurately reflect the retinal topography (Sadda, Keane et al. 2010). In other words, because each volume was acquired independently, it was not necessary to reduce the sampling density in order to minimize the impact of eye movements that might manifest in a single large volume. One important assumption of this technique is that each individual 6 mm x 6 mm thickness map is free from errors. Errors can be caused due to incorrect segmentation of retinal boundaries or due to eye motion during imaging. These cases are of importance as far clinical use of this tool is concerned. The segmentation algorithm used for generating

individual thickness maps might not be able to handle pathological cases leading to segmentation errors. In cases of patients with nystagmus (involuntary rapid eye motion) eye motion will affect the OCT scans which will cause errors in the thickness maps. We used the affine transformation for montaging of the thickness maps so as to keep the distortion of the thickness values to a minimum. As expected the standard deviation of thickness value is in the range of 20mm-60mm near the vessel arcades, the macular region and areas around the nerve head. The standard deviation of thickness falls out as we start moving towards the periphery.

As has been the case over the past few years, OCT technology is changing rapidly. High-speed research-grade systems capable of acquiring up to 1.3 million A-scans per second have been reported (Potsaid, Gorczynska et al. 2008; Torti, Považay et al. 2009; Bonin, Franke et al. 2010; Potsaid, Baumann et al. 2010) (compared to current commercial speeds of ~40,000 A-scans per second). Such improvements, if realized in a commercial system, could provide clinicians with similar wide-field views of retinal thickness as those reported here. Regardless of whether they are generated using software approaches like ours, or future hardware improvements, these wide-field thickness maps are likely to be of significant value. A number of studies have investigated disease progression and treatment potential in individuals with inherited retinal degenerations by comparing manually generated wide-field thickness maps with normal controls (Aleman, Cideciyan et al. 2007; Jacobson, Cideciyan et al. 2007; Jacobson, Aleman et al. 2009).

As segmentation algorithms improve, our method could be expanded to sub-layer maps such as RNFL and establish a normative map for each layer. Data from pathological

subjects can be examined for pathologies by comparing them with the normative average and standard deviation maps. Before these maps could be useful clinically, it is important that we establish normative databases. Given the reported racial and gender variability in foveal morphology (Wagner-Schuman, Dubis et al. 2010), racial variability in optic nerve head morphology (Girkin 2008), and variability in the lateral magnification of OCT scans due to variation in ocular biometrics, it is important that databases take into account such factors in order to ensure their greatest degree of sensitivity and specificity in detecting subtle changes in retinal or sub-layer thickness. Initial results provided here demonstrate a high degree of variability in wide-field maps of retinal thickness, providing the foundation for the creation of a normative database. Such a database could be used to compare future wide-field maps, regardless of whether they were obtained using a software approach like ours or via improved hardware.

5.2 Volume stitching

Zawadzki et al. (2008, 2009) described a volume stitching software which was used for creating large FOV retinal OCT and adaptive optics (AO)-OCT volumes from smaller high density sub-volumes. The software however required manual translation of the sub-volumes in three dimensions in order to align them to each other. In this study we used phase-correlation measure to the translation parameters in three-dimensions. We also corrected for rotational error between two volumes in the x-y plane using PPFT on individual overlapping frames. This work assumed no rotational motion in the z plane. Using 3D PPFT the rotational axis can be recovered but currently the algorithm is computationally expensive for large volume data. From the table 1 it can be seen that a

B-scan is taken every certain number of microns so it is apparent that scans from adjacent overlapping volumes may not exactly overlap. This can be solved by finding translations with sub-pixel accuracy. In this work we avoided sub-pixel registration as it would require interpolation of B-scans reducing the integrity of the scans. Peripheral retinal regions beyond 10mm radius from the fovea have relatively uniform OCT scans and thickness. For stitching these regions, the algorithm can be improved to find the correct global translation parameters by selecting regions of interest (ROI) on known overlapping areas of scans.

Further improvements could be realized by simply stitching together overlapping volumes and then segmenting them to create a wide-field thickness map and corresponding large field-of-view B scan, rather than utilizing thickness data from the individual volumes. However, as thickness data has been shown to be reliable and reproducible and is readily available off of most existing SD-OCT systems, it provided a convenient way to demonstrate proof-of-principle in generating these data. The wide-field volume and thickness map data can be combined to provide a comprehensive tool for studying central and peripheral regions of the retina. Although the clinical utility of tool is yet to be tested, we believe that this tool will aid in providing quantitative measurements for evaluating retinal pathologies.

BIBLIOGRAPHY

Abramoff, M. D., P. J. Magelhaes, et al. (2004). Image processing with ImageJ. *Biophotonics International* 11(7): 36-42.

Aleman, T. S., A. V. Cideciyan, et al. (2007). Inner retinal abnormalities in X-linked retinitis pigmentosa with RPGR mutations. *Invest Ophthalmol Vis Sci* 48(10): 4759-4765.

Asrani, S., S. Zou, et al. (1999). Noninvasive mapping of the normal retinal thickness at the posterior pole. *Ophthalmol* 106: 269-273.

Averbuch, A., R. Coifman, et al. (2006). Fast and accurate polar Fourier transform. *Appl Comput Harmon A* 21(2): 145-167.

Bailey, D. H. and P. N. Swarztrauber (1991). The Fractional Fourier Transform and Applications. *SIAM Review* 33(3): 389-404.

Berson, E. L. (1993). Retinitis Pigmentosa: The Friedenwald Lecture. *Invest Ophthalmol Vis Sci* 34(5): 1659-1676.

Besl, P. J. and N. D. McKay (1992). A Method for Registration of 3-D Shapes. *IEEE Tran Patt Anal* 14(2): 239-256.

Bonin, T., G. Franke, et al. (2010). In vivo Fourier-domain full-field OCT of the human retina with 1.5 million A-lines/s. *Opt Lett* 35(20): 3432-3434.

Borgefors, G. (1984). Distance transformations in arbitrary dimensions. *Comput Vision Graph* 27(3): 321-345.

Bressler, N. M., S. B. Bressler, et al. (1988). Age-related macular degeneration. *Surv Ophthalmol* 32(6): 375-413.

Cense, B., N. Nassif, et al. (2004). Ultrahigh-resolution high-speed retinal imaging using spectral-domain optical coherence tomography. *Opt Express* 12(11): 2435-2447.

Chan, A., J. S. Duker, et al. (2006). Normal macular thickness measurements in healthy eyes using Stratus optical coherence tomography. *Arch Ophthalmol* 124(2): 193-198.

Chou, N., J. A. Izatt, et al. (2009). Generalized pseudo-polar Fourier grids and applications in registering ophthalmic optical coherence tomography images. *Proceedings of the 43rd Asilomar conference on Signals, systems and computers*. Pacific Grove, California, IEEE Press**:** 807-811.

Congdon, N., B. O'Colmain, et al. (2004). Causes and prevalence of visual impairment among adults in the United States. *Arch Ophthalmol* 122(4): 477-485.

Congdon, N. G., D. S. Friedman, et al. (2003). Important causes of visual impairment in the world today. *JAMA* 290(15): 2057-2060.

Delori, F. C., E. S. Gragoudas, et al. (1977). Monochromatic ophthalmoscopy and fundus photography. The normal fundus. *Arch Ophthalmol* 95(5): 861-868.

Drexler, W. (2004). Ultrahigh-resolution optical coherence tomography. *J Biomed Opt* 9(1): 47-74.

Drexler, W. (2007). Cellular and functional optical coherence tomography of the human retina. *Invest Ophthalmol Vis Sci* 48(12): 5340-5351.

Drexler, W., U. Morgner, et al. (2001). Ultrahigh-resolution ophthalmic optical coherence tomography. *Nature Medicine* 7(4): 502-507.

Ellwein, L. B. and C. J. Urato (2002). Use of eye care and associated charges among the Medicare population: 1991-1998. *Arch Ophthalmol* 120(6): 804-811.

Fercher, A. F., C. K. Hitzenberger, et al. (1993). In vivo optical coherence tomography. *Am J Ophthalmol* 116: 113-114.

Fitzpatrick, J. M., J. B. West, et al. (1998). Predicting error in rigid-body point-based registration. *IEEE Trans Med Image* 17(5): 694-702.

Foroosh, H., J. B. Zerubia, et al. (2002). Extension of phase correlation to subpixel registration. *IEEE Trans Image Process* 11(3): 188-200.

Fritsche, P., R. van der Heijde, et al. (2002). Retinal thickness analysis(RTA): an objective method to assess and quantify the retinal thickness in healthy controls and in diabetics without diabetic retinopathy. *Retina* 22(6): 768-771.

Geitzenauer, W., C. K. Hitzenberger, et al. (2011). Retinal optical coherence tomography: past, present and future perspectives. *Br J Ophthalmol* 95(2): 171-177.

Girkin, C. A. (2008). Differences in optic nerve structure between individuals of predominantly African and European ancestry: Implications for disease detection and pathogenesis. *Clin Ophthalmol* 2(1): 65-69.

Goshtasby, A. (2005). 2-D and 3-D image registration for medical, remote sensing, and industrial applications. Hoboken, NJ, J. Wiley & Sons.

Grover, S., R. K. Murthy, et al. (2009). Normative data for macular thickness by high-definition spectral-domain optical coherence tomography (spectralis). *Am J Ophthalmol* 148(2): 266-271.

Hajnal, J. V., D. L. G. Hill, et al. (2001). Medical Image Registration. Florida, CRC Press LLC.

Hee, M. R., C. R. Baumal, et al. (1996). Optical coherence tomography of age-related macular degeneration and choroidal neovascularization. *Ophthalmol* 103(8): 1260-1270.

Hee, M. R., C. A. Puliafito, et al. (1995). Quantitative assessment of macular edema with optical coherence tomography. *Arch Ophthalmol* 113(8): 1019-1029.

Holz, F. G., C. Bellman, et al. (2001). Fundus autofluorescence and development of geographic atrophy in age-related macular degeneration. *Invest Ophthalmol Vis Sci* 42(5): 1051-1056.

Hoyt, W. F., L. Frisen, et al. (1973). Fundoscopy of Nerve Fiber Layer Defects in Glaucoma. *Invest Ophthalmol Vis Sci* 12(11): 814-829.

Huang, D., E. A. Swanson, et al. (1991). Optical coherence tomography. *Science* 254(5035): 1178-1181.

Jacobson, S. G., T. S. Aleman, et al. (2005). Identifying photoreceptors in blind eyes caused by RPE65 mutations: Prerequisite for human gene therapy success. *Proc Natl Acad Sci USA* 102(17): 6177-6182.

Jacobson, S. G., T. S. Aleman, et al. (2009). Disease boundaries in the retina of patients with Usher syndrome caused by MYO7A gene mutations. *Invest Ophthalmol Vis Sci* 50(4): 1886-1894.

Jacobson, S. G., A. V. Cideciyan, et al. (2007). Leber Congenital Amaurosis caused by an RPGRIP1 mutation shows treatment potential. *Ophthalmol* 114(5): 895-898.

Jennings, B. J. and D. E. Mathews (1994). Adverse reactions during retinal fluorescein angiography. *J Am Optom Assoc* 65(7): 465-471.

Johnson, C. A. (1995). The Glenn A. Fry Award Lecture: Early Losses of Visual Function in Glaucoma. *Optometry Vision Sci* 72(6): 359-370.

Keller, Y., A. Averbuch, et al. (2005). Pseudopolar-based estimation of large translations, rotations, and scalings in images. *IEEE Trans Image Proc* 14(1): 12-22.

Keller, Y., A. Averbuch, et al. (2005). Algebraically Accurate Volume Registration Using Euler's Theorem and the 3-D Pseudo-Polar FFT. *Proceedings of the 2005 IEEE Computer Society Conference on Computer Vision and Pattern Recognition (CVPR'05)* IEEE Computer Society. 2**:** 795-800.

Keller, Y., Y. Shkolnisky, et al. (2005). The angular difference function and its application to image registration. *IEEE Trans Pattern Anal* 27(6): 969-976.

Keller, Y., Y. Shkolnisky, et al. (2006). Volume Registration Using the 3-D Pseudopolar Fourier Transform. *IEEE Trans Signal Proc* 54(11): 4323-4331.

Kuglin, C. D. and D. C. Hines (1975). The phase correlation image alignment method. *IEEE Conf Cybern Soc*.

Lin, D. Y., M. S. Blumenkranz, et al. (2002). The sensitivity and specificity of single-field nonmydriatic monochromatic digital fundus photography with remote image interpretation for

diabetic retinopathy screening: a comparison with ophthalmoscopy and standardized mydriatic color photography. *Am J Ophthalmol* 134(2): 204-213.

Maes, F., A. Collignon, et al. (1997). Multimodality image registration by maximization of mutual information. *IEEE Trans Med Imaging* 16(2): 187-198.

Maintz, J. B. and M. A. Viergever (1998). A survey of medical image registration. *Med Image Anal* 2(1): 1-36.

Munoz, B., S. K. West, et al. (2000). Causes of Blindness and Visual Impairment in a Population of Older Americans: The Salisbury Eye Evaluation Study. *Arch Ophthalmol* 118(6): 819-825.

Mwanza, J. C., J. D. Oakley, et al. (2011). Ability of cirrus HD-OCT optic nerve head parameters to discriminate normal from glaucomatous eyes. *Ophthalmol* 118(2): 241-248 e241.

Pelizzari, C. A., G. T. Chen, et al. (1989). Accurate three-dimensional registration of CT, PET, and/or MR images of the brain. *J Comput Assist Tomogr* 13(1): 20-26.

Polaczek-Krupa, B. and I. Grabska-Liberek (2006). Application of retinal thickness analyzer (RTA) in diagnosis and treatment monitoring in retinal diseases. *Klin Oczna* 108(10-12): 452-456.

Potsaid, B., B. Baumann, et al. (2010). Ultrahigh speed 1050nm swept source/Fourier domain OCT retinal and anterior segment imaging at 100,000 to 400,000 axial scans per second. *Opt Express* 18(19): 20029-20048.

Potsaid, B., I. Gorczynska, et al. (2008). Ultrahigh speed spectral / Fourier domain OCT ophthalmic imaging at 70,000 to 312,500 axial scans per second. *Opt Express* 16(19): 15149-15169.

Preibisch, S., S. Saalfeld, et al. (2009). Globally optimal stitching of tiled 3D microscopic image acquisitions. *Bioinformatics* 25(11): 1463-1465.

Quigley, H. A. (2005). Glaucoma: Macrocosm to Microcosm The Friedenwald Lecture. *Invest Ophthalmol Vis Sci* 46(8): 2663-2670.

Reddy, B. S. and B. N. Chatterji (1996). An FFT-based technique for translation, rotation, and scale-invariant image registration. *IEEE Trans Image Process* 5(8): 1266-1271.

Sadda, S. R., F. B. Keane, et al. (2010). Impact of scanning density on measurements from spectral domain optical coherence tomography. *Invest Ophthalmol Vis Sci* 51(2): 1071-1078.

Schuman, J. S., M. R. Hee, et al. (1995). Optical coherence tomography: a new tool for glaucoma diagnosis. *Curr Opin Ophthalmol* 6(2): 89-95.

Shahidi, M., N. P. Blair, et al. (2002). Retinal topography and thickness mapping in atrophic age related macular degeneration. *Br J Ophthalmol* 86(6): 623-626.

Stewart, C. V. (2009). The i2k Align and i2k Align retina toolkits: Correspondences and transformations, Dual Align LLC.

Swanson, E. A., J. A. Izatt, et al. (1993). In vivo retinal imaging by optical coherence tomography. *Opt Lett* 18: 1864-1866.

Szeliski, R. (2006). Image alignment and stitching: a tutorial. *Found Trends Comput Graph Vis* 2(1): 1-104.

Tanito, M., N. Itai, et al. (2004). Reduction of posterior pole retinal thickness in glaucoma detected using the Retinal Thickness Analyzer. *Ophthalmol* 111(2): 265-275.

Torti, C., B. Považay, et al. (2009). Adaptive optics optical coherence tomography at 120,000 depth scans/s for non-invasive cellular phenotyping of the living human retina. *Opt Express* 17(22): 19382-19400.

Wagner-Schuman, M., A. M. Dubis, et al. (2010). Race- and sex-related differences in retinal thickness and foveal pit morphology. *Invest Ophthalmol Vis Sci* 52: 625-634.

West, S. K., B. Munoz, et al. (1997). Function and visual impairment in a population-based study of older adults. The SEE project. Salisbury Eye Evaluation. *Invest Ophthalmol Vis Sci* 38(1): 72-82.

Wojtkowski, M. (2010). High-speed optical coherence tomography: basics and applications. *Appl Opt* 49(16): D30-61.

Wojtkowski, M., R. Leitgeb, et al. (2002). In vivo human retinal imaging by Fourier domain optical coherence tomography. *J Biomed Opt* 7(3): 457-463.

Wojtkowski, M., V. Srinivasan, et al. (2005). Three-dimensional retinal imaging with high-speed ultrahigh-resolution optical coherence tomography. *Ophthalmol* 112(10): 1734-1746.

Wolberg, G. and S. Zokai (2000). Robust image registration using log-polar transform. *IEEE Image Proc* 1: 493-496.

Yang, G., C. V. Stewart, et al. (2007). Registration of challenging image pairs: initialization, estimation, and decision. *IEEE Trans Pattern Anal* 29(11): 1973-1989.

Zawadzki, R. J., S. S. Choi, et al. (2009). Cellular resolution volumetric in vivo retinal imaging with adaptive optics-optical coherence tomography. *Opt Express* 17(5): 4084-4094.

Zawadzki, R. J., A. R. Fuller, et al. (2008). Improved representation of retinal data acquired with volumetric Fd-OCT: co-registration, visualization, and reconstruction of a large field of view. *Proc SPIE*. 6844**:** 68440C.

Zeimer, R., M. Shahidi, et al. (1996). A new method for rapid mapping of the retinal thickness at the posterior pole. *Invest Ophthalmol Vis Sci* 37(10): 1994-2001.

Zitova, B., J. Flusser, et al. (2005). Image Registration: A survey and recent advances. *IEEE Image Proc*.